Snow Water Equivalent Change Mapping from Slope Correlated InSAR Phase Variations

Jayson Eppler[1], Bernhard Rabus[1], and Peter Morse[2]

[1]School of Engineering Science, Simon Fraser University, Burnaby, BC V5A 1S6, Canada
[2]Geological Survey of Canada, Natural Resources Canada, Ottawa, ON, K1A 0E8, Canada

Correspondence: Jayson Eppler (jaysone@sfu.ca)

Abstract. Area-based measurements of snow water equivalent (SWE) are important for understanding earth system processes such as glacier mass balance, winter hydrological storage in drainage basins and ground thermal regimes. Remote sensing techniques are ideally suited for wide-scale area-based mapping with the most commonly used technique to measure SWE being passive-microwave, which is limited to coarse spatial resolutions of 25 km or greater, and to areas without significant topographic variation. Passive-microwave also has a negative bias for large SWE. Repeat-pass synthetic aperture radar interferometry (InSAR) as an alternate technique allows measurement of SWE change at much higher spatial resolution. However, it has not been widely adopted because: (1) the phase unwrapping problem has not been robustly addressed, especially for interferograms with poor coherence and; (2) SWE change maps scaled directly from repeat-pass interferograms are not an absolute measurement but contain unknown offsets for each contiguous coherent area. We develop and test a novel method for repeat-pass InSAR based dry-snow SWE estimation that exploits the sensitivity of the dry-snow refraction-induced InSAR phase to topographic variations. The method robustly estimates absolute SWE change at spatial resolutions of <1 km, without the need for phase unwrapping. We derive a quantitative signal model for this new SWE change estimator and identify the relevant sources of bias. The method is demonstrated using both simulated SWE distributions and a 9-year RADARSAT-2 spotlight-mode dataset near Inuvik, NWT, Canada. SWE results are compared to in situ snow survey measurements and estimates from ERA5 reanalysis. Our method performs well in high-relief areas and in areas with high SWE (>150 mm), thus providing complementary coverage to other passive- and active-microwave based SWE estimation methods. Further, our method has the advantage of requiring only a single wavelength band and thus can utilize existing spaceborne synthetic aperture radar systems. In application, a first order analysis of SWE trends within three drainage basins suggests that differences between basin-level accumulations are a function of major landcover types, and that re-vegetation following a forest-tundra fire that occurred over 50 years ago continues to affect the spatial distribution of SWE accumulation in the study area.

1 Introduction

Snow melt is one of the greatest sources of water in snow-affected areas, snow accumulation on glaciers is critical to their mass balance and longevity, and snow cover variation is a dominant control on ground thermal regimes in cold regions, thus quantification of snowpack conditions is essential to understanding the role of snow on earth system processes. Snow water equivalent (SWE) is the amount of liquid-water in a vertical column of snow and is a key parameter of snowpack conditions.

30 Traditionally, SWE variation over space and time is interpolated from sparse point-based measurements, which generally show significant spatial variation due to factors such as topography and vegetation, and temporal bias if the acquisition of each set of points is distributed over a range of dates (ideally the SWE measurement is carried out over a short time span to limit within-set variation due to changing meteorological conditions). Further bias may be introduced if different point-based methods are integrated together to estimate SWE over large areas. To avoid biases arising from the interpolation of

35 point-based measurements of typical snow packs, several remote sensing techniques have been developed for wide-scale, area-based determination of SWE. With precipitation regimes changing globally under persistent climate change (Pachauri et al., 2015), remote sensing techniques offer the potential to monitor hydrological conditions over vast areas of cold regions where point-based measurements are typically sparse, collected intermittently, and with a range of techniques.

Snow depth, used to infer SWE when integrated with snow density, has been determined using surface elevation models

40 developed using LiDAR as well as structure-from-motion (optical photogrammetry) systems, either by differential repeat-pass measurement or comparison with a pre-existing snow-free reference elevation model (Deems et al., 2013; Nolan et al., 2015). However, as these systems are presently only feasible on airborne platforms they have not yet been used for repeated, wide-scale SWE mapping, which is required to substantively improve hydrological monitoring. Alternatively, spaceborne systems are designed for repeated wide-scale monitoring, and both passive- and active-microwave methods to determine SWE have

45 been demonstrated (Saberi et al., 2020; Lemmetyinen et al., 2018). However, despite the potential for spaceborne microwave determination of SWE, there are key limitations inherent within each of the current approaches that affect the sensitivity and uncertainty of the measurements and prevent adoption of the methods for wide-scale SWE monitoring.

Passive-microwave SWE estimation is based on the measurement of the attenuation of Earth-emitted thermal microwave radiation by an overlaying snowpack (Kunzi et al., 1982). It has been implemented on several spaceborne systems, generating

50 global SWE maps with a revisit frequency of up to daily (e.g., Takala et al., 2011). However, the passive-microwave method has severe limitations (Takala et al., 2011). These are: (1) increased uncertainty for larger SWE (> 150 mm) due to attenuation saturation; (2) dependence on snow properties such as grain-size distribution; (3) signal contamination from topographic variation, which restricts the method to low-relief regions; and (4) coarse spatial resolution; e.g. >25 km in the case of Advanced Microwave Scanning Radiometer (AMSR)–E daily products.

55 In contrast to passive systems, active-microwave SWE estimation methods are based on measuring radiation emitted from a synthetic aperture radar (SAR) system that has returned after having interacted with the snowpack. One method that promises high spatial resolution is dual-frequency active microwave estimation, which measures total SWE in a single pass of the SAR based on the difference between the volume backscatter power returned by the snowpack by two radio-frequency bands

(e.g. X-band versus Ku-band). The dual-band requirement of this method currently limits it to ground-based and airborne
implementations, although method-capable spaceborne missions have been proposed (e.g., Rott et al., 2012; Derksen et al.,
2019). Limitations of this method include a dependence on grain-size distribution of the snow crystals and an applicability
restriction to predominately dry-snow and vegetation-free areas (Oveisgharan et al., 2020).

Active-microwave based estimation of dry-snow SWE change can also be achieved through repeat-pass SAR interferometry
(InSAR) by exploiting the phase contribution that results from refraction in dry-snow (Guneriussen et al., 2001; Deeb et al.,
2011; Leinss et al., 2015). This method measures temporal SWE changes between repeat acquisitions rather than total SWE; the
latter must be inferred later through integrating the SWE change maps over time. Performance depends on sensing frequency:
higher frequencies (e.g. X-band compared to C- or L-band) have better phase sensitivity to SWE change but are more prone
to temporal decorrelation and to interference from volume scattering. This method promises high spatial resolution but it is
constrained by the following requirements: (1) observability is limited to conditions in space and time with low decorrelation;
(2) a spatial reference with known SWE change since the InSAR phase carries an unknown offset; and (3) phase-unwrapping
to resolve 2π ambiguities, which occur in significant number for typical snowpacks (Rott et al., 2003; Leinss et al., 2015).
Conditions for low decorrelation require the absence of significant liquid water content, spatially inhomogeneous changes to
the snow distribution, or strong volume scattering effects. Particularly, due to the need and difficulty of phase unwrapping,
the method has not yet been operationally adopted for wide-scale, repeat monitoring of SWE despite being proposed and
demonstrated over 20 years ago (Guneriussen et al., 2001).

The Delta-K method for SWE estimation (Engen et al., 2004) is a variant of the InSAR method that differences the InSAR
dry-snow phase between two radar carrier frequency sub-bands. This approach has the benefits of not requiring a spatial phase
reference and eliminates the need for phase unwrapping, however, these are at the cost of a much-reduced sensitivity that
requires substantial spatial smoothing to suppress the noise, which results in only coarse spatial resolution SWE estimates. For
example, Engen et al. (2004) report 100 mm SWE accuracy at 10 km resolution when applying the method to ERS-1 (C-band)
data.

We hypothesize that it is possible to overcome some of the key limitations of repeat-pass InSAR for dry-snow SWE change
estimation, at the cost of only moderately reduced spatial resolution, by exploiting the sensitivity of the dry-snow refractive
InSAR phase signal to topographic slope. Our objective is to develop a spatial analysis method for repeat-pass InSAR that
allows for unambiguous SWE change estimation directly from the wrapped InSAR phase without need for a spatial phase
reference and phase unwrapping, and that is insensitive to other InSAR phase components not correlated with topographic
slope at the scale of the output resolution (size of SWE estimation kernel). The novel method is conceptually similar to
established methods for estimating temporal changes of the layered tropospheric delay in repeat pass InSAR (e.g., Lin et al.,
2010), and offers the same benefits as the Delta-K method but with substantially better sensitivity and spatial resolution for
most terrains.

Our paper is organized as follows: first we describe the multi-year RADARSAT-2 dataset and ancillary data that we use to
demonstrate and test the novel method. We then develop a quantitative model for the repeat-pass InSAR phase resulting from
dry-snow refraction that explicitly considers topographic slope variation. Subsequently, we introduce a spatial-correlation-

based method for estimating SWE change from a repeat-pass interferogram, first from a locally unwrapped spatial phase signal
and then directly from the wrapped phase. We compare the expected performance and precision of our method to that of the
Delta-k method. We then examine sources of estimation error in our new approach and establish their relative significance.
Sources considered include the effects of (1) violated model assumptions; (2) other InSAR phase components and; (3) digital
elevation model (DEM) errors. Next, we show results from applying our novel SWE retrieval method to the full RADARSAT-
2 InSAR dataset. We discuss these results in the context of several in situ SWE transect surveys located within the imaged
footprint, as well as a mean SWE temporal history estimated by the ERA5 climate reanalysis model. We then present a first
order assessment of the ΔSWE results in the context of landcover type, fire history, and three drainage basins with the study
area. Finally, we present our conclusions with a focus on the feasibility of our method for SWE change mapping in the context
of existing methods.

2   Description of Dataset and Study Site

The InSAR dataset used for this study is a time series of 120 RADARSAT-2 Spotlight-A (RS2-SLA) descending-pass single-
look complex (SLC) images spanning the period 2012-02-22 to 2021-01-29 at 24-day intervals; nearly continuously with only
a few time gaps (Table 1). The study area, situated in Northwest Territories, Canada, at the eastern margin of the Mackenzie
Delta, about 120 km south of the Beaufort Sea coast, covers 238 km^2 defined by the SAR imaging footprint and it includes the
town of Inuvik. The mean backscatter amplitude image for the dataset is shown in Fig. 1a.

Table 1. Parameters for the RADARSAT-2 dataset used for this study.

Parameter	Value
Mode	Spotlight-A
Pass direction	Descending
Scene center (Lat., Long.)	68.35°N, -133.65°E
Date range	2012-02-22 to 2021-01-29
Number of images	120
Repeat interval	24 days
Radar frequency	5.405 GHz
Range bandwidth	100.0 MHz
Incidence angle	49.1°
Pixel spacing (slant range × azimuth)	1.33 m × 0.41 m
Image samples (range × azimuth)	12230 × 27064
Image size (ground range × azimuth)	22 km × 11 km

Our proposed SWE change estimation method requires knowledge of the variation in topographic slope. To derive the slope,
we used a 12 m spatial resolution TanDEM-X digital elevation model (DEM) provided by the German Aerospace Centre
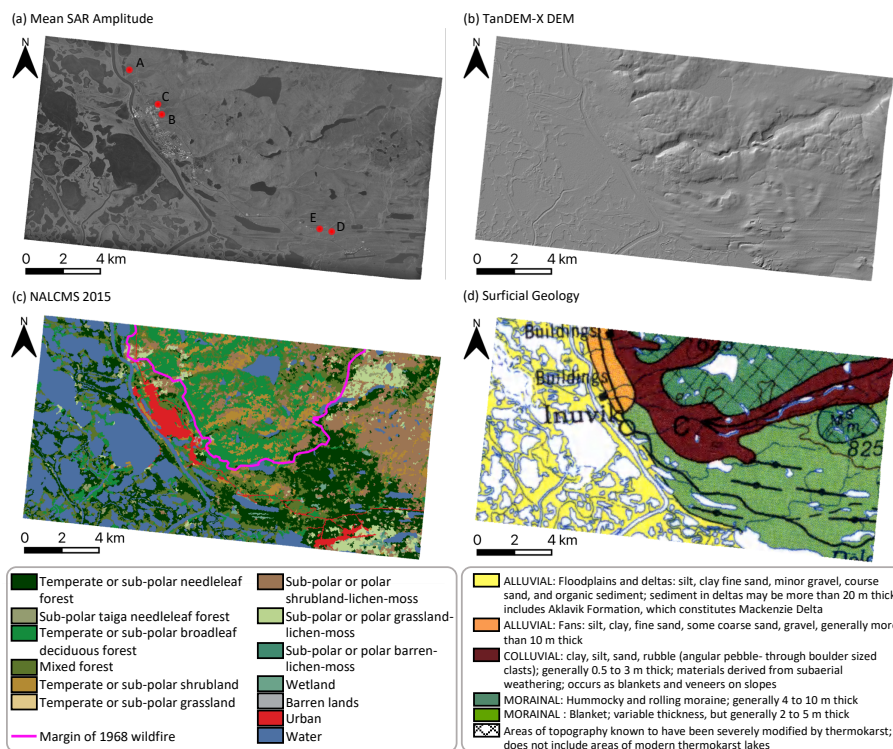
Figure 1. (a) Mean amplitude of all co-registered RS2-SLA images, (b) hill-shaded TanDEM-X DEM (DLR 2016) over the SAR footprint, (c) North America Land Change Monitoring System (2015) classification map (provided jointly by Natural Resources Canada, Comisión Nacional para el Conocimiento y Uso de la Biodiversidad, Comisión Nacional Forestal, Instituto Nacional de Estadística y Geografía, and the U.S. Geological Survey, 2015) showing spatial variation of land cover and superimposed with margin of 1968 wildfire (discussed in Sect. 7), (d) surficial geology map of the area from Rampton (1987) © Her Majesty the Queen in Right of Canada, as represented by the Minister of Energy, Mines and Resources Canada, 1987. Positions labelled A-E in panel (a) refer to the snow surveys described in Sect. 6.2.

(DLR). This DEM was derived from source images acquired between 2011-01-13 and 2014-08-08 including snow-season acquisitions so some snow-related bias may affect the estimated elevations. Regarding DEM accuracy, our method described in Sect. 4 depends on local slope variations and is therefore sensitive only to local relative rather than absolute DEM errors.

115   Wessel et al. (2018) report a root-mean-square-error (RMSE) of 1.8 m for TanDEM-X elevations over forested terrain. We also used this DEM for InSAR topographic phase correction and as an input for later snow transport modelling. The DEM shows that Mackenzie Delta (near sea-level) in the eastern portion of the study area has little topographic variation, but to the east of the delta's margin, elevation increases to a maximum of approximately 200 m above mean sea level (Fig. 1b). Several riparian zones drain this upland area towards the delta and create substantial local-scale topographic variation.

120   The study area is south of the treeline and ecologically is broadly categorized as subarctic boreal forest, however, according to the North American Land Change Monitoring System (NALCMS) 2015 dataset, a 30-metre resolution land classification based on Landsat and RapidEye imagery using the methodology described by Latifovic et al. (2017), there is significant

variation in vegetation distribution and density within the study area (Fig. 1c). The upland area east of the delta features forest, shrubland, and grassland, whereas the delta proper is predominantly forested, but is interspersed with areas of shrubs and sedge

125   wetlands (Burn and Kokelj, 2009). There are extensively developed lands in the study area that include the centrally located town of Inuvik, segments of the Inuvik-Tuktoyaktuk highway and the Dempster highway that extend, respectively, northward and westward from the town site, and the Inuvik airport in the southeastern corner of the study footprint.

The study area lies within the (spatially) continuous permafrost region (Heginbottom, 1995; Nguyen et al., 2009). Permafrost is ground that remains at or below 0 °C for two or more years that is overlain by an active layer that thaws seasonally. The

130   permafrost in the study area is commonly ice rich (Burn et al., 2009), and occurs within surficial deposits of several origins that are predominantly unconsolidated (Fig. 1d). As a result of climate warming in the region, permafrost temperatures and active layer thickness are increasing and producing ground surface settlement where there is net thaw of near-surface, ice-rich permafrost (Kokelj et al., 2017; O'Neill et al., 2019).

As shown in Fig. 2, Inuvik normally receives some level of snowfall for all months of the year except July (ECCC, 2021a).

135   The mean annual snowfall is 126 mm water equivalent. For dry-snow conditions, temperatures must remain below freezing; the daily maximum temperatures in Inuvik normally remain below zero for the months of October to April. At upland locations, dry snow in the area is redistributed by wind and large drifts develop in relation to topographic relief and shrub growth; while in the delta proper, forest and shrub vegetation combine with the lack of relief to minimize wind effects on the snow pack (Burn et al., 2009; Mackay and MacKay, 1974; Palmer, 2007; Morse et al., 2012).
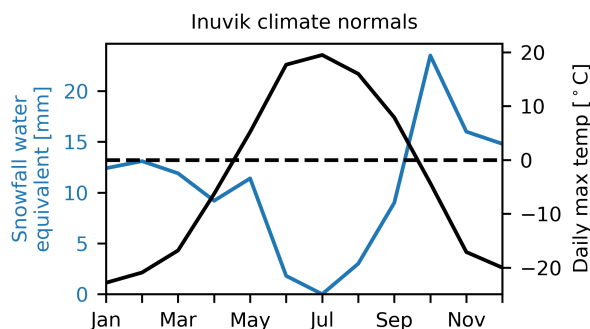
Figure 2. Normal monthly mean snowfall and daily maximum temperature for Inuvik for period of 1985 – 2010.

140   ## 3   Spatial Variations of Repeat-pass InSAR Dry-snow Phase

3.1   Origin of Dry-snow Phase

Guneriussen et al. (2001) first described the method of SAR interferometric repeat-pass SWE change estimation, which we summarize as follows. In the case of a dry homogenous layer of snow over ground, a microwave radar signal will penetrate the snow layer, be scattered at the ground surface and then return through the snow layer. Surface and volume scattering occur

145 at the air-snow interface and within the snowpack respectively, but for sufficiently dry-snow, it can be expected that these contributions will be much less that the primary ground-scattered return. The dry-snow layer has a higher permittivity than air and therefore causes refraction at the air-snow interface, which corresponds to a reduction in the propagation speed of the signal within the snowpack and a corresponding geometric path-length increase as shown in Fig. 3. Compared to the snow free state, the phase of the SAR signal,
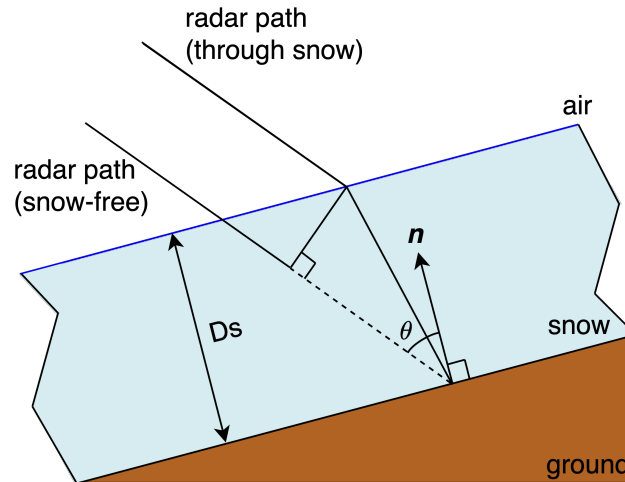
Figure 3. Geometry of refracted ray through a dry snow layer over an inclined ground surface compared to the unrefracted (straight) ray trajectory.

150 $$\Phi_s(\theta) = \frac{4\pi}{\lambda} D_s \left(\sqrt{\epsilon(\rho) - \sin^2\theta} - \cos\theta \right),$$ (1)

increases with both snow density ρ (defined dimensionless as the ratio of the gravimetric densities of snow and water) and snow layer thickness D_s (projected along the local slope surface normal direction $\boldsymbol{n}$). Functional dependency on ρ is via the dielectric permittivity ϵ, with other parameters in Eq.(1) being the local incidence angle θ and the radar wavelength λ.

In the case of a stratified snowpack, Leinss et al. (2015) have shown that the phase contribution is well approximated by a
155 single layer with mean vertical density,

$$\rho \approx \frac{1}{Z_s} \int_0^{Z_s} \rho(z) \mathrm{d}z = \frac{S}{Z_s},$$ (2)

where S is the SWE of the snowpack with depth Z_s (measured vertically). Noting that $Z_s = D_s / \cos\alpha$ where α is the local topographic slope angle, Eqs.(1) and (2) can be combined to provide the explicit linear relation between dry-snow phase and SWE,

$$160 \quad \Phi_s(\theta) = S \frac{4\pi}{\lambda\rho} \, \cos\alpha \left(\sqrt{\epsilon(\rho) - \sin^2\theta} - \cos\theta \right). \tag{3}$$

The relation holds for the general case of repeat-pass interferometric dry-snow phase between any two dry-snow states by replacing total SWE, S, with SWE change, ΔS, and interpreting ρ as the magnitude of the mean density of the removed or added snow layer. As such, ΔS can be either positive or negatively valued and $\rho \geq 0$.

3.2 Dry-snow Phase Dependence on Local Topographic Slope

165   SAR images are formed by focusing complex-valued pulse returns obtained sequentially along a one-dimensional flight track (e.g. satellite orbit segment in the case of spaceborne systems). Each image resolution cell is formed by coherently combining signals received over a finite aperture. The phase contribution due to dry-snow refraction depends on the local incidence angle, which varies along the aperture. The net effect on the focused image phase, however, is well approximated by considering only the Doppler centroid (i.e. beam center) incident angle at the target (Eppler and Rabus, 2021).

170   For a focused image, in a local spatial region with constant topographic slope where incidence angle is uniform (gradual across-swath variations can be neglected) a horizontally uniform snow layer results in a uniform phase. In contrast, a local spatial region with topographic slope variations will generate dry-snow phase variations corresponding to variations in the local incidence angle and projection of the snow depth onto the slope normal.

Figure 4 depicts the topographic modulation of dry-snow snow phase explicitly at foreslope, horizontal, and backslope

175   locations. The local incidence angle is less on the foreslope and becomes greater along the transition towards the backslope. The dry-snow phase increases with incidence angle and therefore this effect causes the phase contribution to increase along the transition from foreslope to backslope.

The projection of the snow depth onto the slope normal scales with the cosine of the slope angle and is therefore greatest in horizontal areas and less on both the foreslope and backslope. Considering Eq.(3) , if the topographic variation within a SAR

180   scene is known, then the spatially variable sensitivity of the dry-snow phase to a uniform SWE layer can be computed as,

$$\xi \doteq \frac{d\Phi_s}{dS} = \frac{4\pi}{\lambda\rho} \, \cos\alpha \left(\sqrt{\epsilon(\rho) - \sin^2\theta} - \cos\theta \right), \tag{4}$$

where we assume that snow density, ρ, is known. A spatially varying change in dry-SWE during a time-interval spanned by two SAR acquisitions will cause a corresponding spatially variable interferometric phase contribution, modulated by the topographic sensitivity,

$$185 \quad \Phi_s = \xi\Delta S. \tag{5}$$

This effect is depicted in Fig. 5, which shows ξ computed over the RS2-SLA spatial footprint and a late snow-season interferogram which shows spatial phase variations that are correlated with ξ.
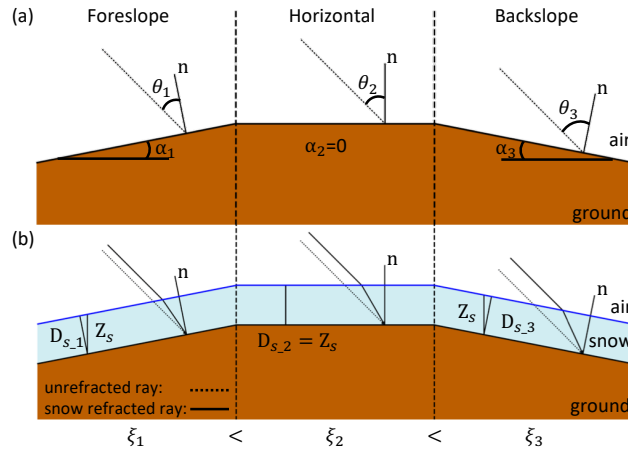
Figure 4. Time evolution of dry-snow refraction geometry for different topographic slopes. (a) depicts a snow free hill divided into foreslope, horizontal (i.e. hilltop) and backslope with a fixed incident radar direction and it shows that the local incidence angle increases from foreslope to backslope. (b) depicts the same hill with the addition of a dry-snow layer and shows the corresponding refracted ray geometry. Refraction increases from foreslope to backslope. Also illustrated is a reduction of the slope-normal projected snow depth, D_s with increasing slope angle, α, while vertical snow depth is constant.

4 Estimation Method

4.1 Estimating Absolute ΔSWE by Exploiting Topographic Variation

190 According to Eq.(5), if the absolute unwrapped dry-snow phase, Φ_s, can be recovered, then the spatially varying SWE change can be directly estimated at the same spatial resolution as the interferogram. However, this requires phase unwrapping which can be difficult for snow covered interferograms both due to aliasing and local incoherence of the InSAR phase. Furthermore, although the unwrapped-phase can be determined, the phase offset is unknown. One or more reference targets with known SWE change (ΔSWE) are required to estimate the offset. For these reasons, direct estimation of ΔSWE from interferograms

195 is not straightforward. However, we suggest that the effect of topographic modulation of dry-SWE phase described in Sect. 3.2 allows an absolute estimate without requiring phase unwrapping or knowing the phase offset.

Consider a local estimation window, sufficiently large to contain some topographic slope variation. The phase within this window consists of the superposition of the dry snow phase contribution and other phase components (e.g., due to decorrelation, surface displacement, imperfect topographic correction, soil moisture, or tropospheric delay). For the purposes of estimating

200 dry-snow, we treat the other phase components as a single error phase term, Φ_e. Due to the difficulty of phase unwrapping and offset estimation we assume that only the locally de-meaned superposition phase is available,

$$\tilde{\Phi} = \Phi - \langle \Phi \rangle = \Phi_s - \langle \Phi_s \rangle + \Phi_e - \langle \Phi_e \rangle, \tag{6}$$
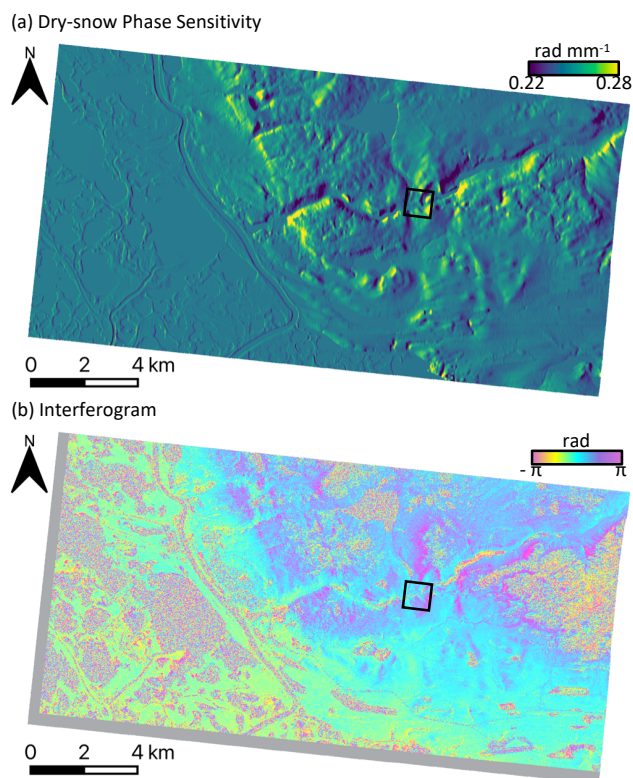
Figure 5. (a) Dry-snow phase sensitivity, ξ, for the RS2-SLA geometry and assuming relative snow density, $\rho = 0.3$, (b) Topo-corrected 24-day interferogram 20120317_20120410 showing spatial correlation with dry-snow phase sensitivity in the upland areas (eastern part of image footprint). The rectangular inset area corresponds to the example shown in Fig. 6.

where $\langle \cdot \rangle$ denotes the mean over the window. Initially, for simplicity we assume also that phase variation within the window is limited to a 2π ambiguity interval so that (unwrapped) $\tilde{\Phi}$ is easily obtained from the corresponding wrapped-phase, ϕ, within the window,

$$\tilde{\Phi} = \angle \left(\left\langle e^{\mathrm{j}\phi} \right\rangle^* e^{\mathrm{j}\phi} \right), \tag{7}$$

where * denotes complex conjugation.

The unknown spatially variable SWE change within the window can then be described by

$$\Delta S = \langle \Delta S \rangle + \tilde{\Delta S}, \tag{8}$$

where $\tilde{\Delta S}$ corresponds to the zero-mean spatially variable component of the SWE change. The known topographic dry-snow phase sensitivity can be similarly decomposed as

$$\xi = \langle \xi \rangle + \tilde{\xi}. \tag{9}$$

Substituting Eqs.(8) and (9) into Eq.(5) and expanding yields

$$\Phi_s = \langle \xi \rangle \langle \Delta S \rangle + \langle \xi \rangle \tilde{\Delta S} + \langle \Delta S \rangle \tilde{\xi} + \tilde{\xi} \tilde{\Delta S}. \tag{10}$$

215   Substituting Eq.(10) into Eq.(6) and noting that $\left\langle \tilde{\Delta S} \right\rangle = \left\langle \tilde{\xi} \right\rangle = 0$ gives,

$$\tilde{\Phi} = \langle \Delta S \rangle \tilde{\xi} + \langle \xi \rangle \tilde{\Delta S} + \tilde{\xi} \tilde{\Delta S} - \left\langle \tilde{\xi} \tilde{\Delta S} \right\rangle + \Phi_e - \langle \Phi_e \rangle. \tag{11}$$

Assuming that the first term, $\langle \Delta S \rangle \tilde{\xi}$, is the dominant component, we introduce the following correlation-based estimator for $\langle \Delta S \rangle$,

$$\widehat{\Delta S} := \frac{\left\langle \tilde{\xi} \tilde{\Phi} \right\rangle}{\left\langle \tilde{\xi}^2 \right\rangle} = \langle \Delta S \rangle + \frac{1}{\left\langle \tilde{\xi}^2 \right\rangle} \left[\langle \xi \rangle \left\langle \tilde{\xi} \tilde{\Delta S} \right\rangle + \left\langle \tilde{\xi}^2 \tilde{\Delta S} \right\rangle + \left\langle \tilde{\xi} \Phi_e \right\rangle \right]. \tag{12}$$

220   This estimator correlates the observable de-meaned phase $\tilde{\Phi}$ with the known topographic variation in dry-SWE phase sensitivity $\tilde{\xi}$. The estimator relies on the assumption that the horizontal SWE change distribution is uniform within the window and that other interferometric phase components are uncorrelated with $\tilde{\xi}$. The bias of $\widehat{\Delta S}$ with respect to $\langle \Delta S \rangle$ is given by

$$E\left(\widehat{\Delta S}\right) - \langle \Delta S \rangle = \frac{1}{\left\langle \tilde{\xi}^2 \right\rangle} \left[\langle \xi \rangle E\left(\left\langle \tilde{\xi} \tilde{\Delta S} \right\rangle\right) + E\left(\left\langle \tilde{\xi}^2 \tilde{\Delta S} \right\rangle\right) + E\left(\left\langle \tilde{\xi} \Phi_e \right\rangle\right) \right], \tag{13}$$

where $E(\cdot)$ denotes the expectation. Therefore, $\widehat{\Delta S}$ is biased by horizontal SWE change variations, $\tilde{\Delta S}$, that are systematically
225   correlated with either $\tilde{\xi}$ or $\tilde{\xi}^2$, and by other interferometric phase components systematically correlated with $\tilde{\xi}$. The significance of the different bias terms is examined in Sect. 5.2 and Sect. 5.3.

4.2   Wrapped-phase ('SlopeVar') Estimator

The estimator defined in Eq.(12) requires the demeaned unwrapped-phase $\tilde{\Phi}$ within the spatial window of consideration and we have assumed so far that this can be obtained from the wrapped phase through Eq.(7) implicitly assuming phase variations
230   in the window are limited to a maximum of 2π. As shown by Just and Bamler (1994), decorrelation to any degree results in a per-target phase distribution that is not bound by the $\pm\pi$ interval and so this condition is never strictly met. Except for high coherence areas with limited short-scale phase variation, the phase within the window must either be unwrapped or an alternate wrapped-phase version of the estimator is required.

Here we propose such an alternate estimator (which we denote the 'SlopeVar' estimator) that uses periodogram optimization
235 to iteratively estimate $\langle \Delta S \rangle$, using the set of wrapped phases under the window,

$$\widehat{\Delta S}_{\mathrm{w}} = \underset{\Delta S_{\mathrm{w}}}{\mathrm{argmax}} \left| \left\langle e^{j\left(\phi - \Delta S_{\mathrm{w}}\tilde{\xi}\right)} \right\rangle \right|. \tag{14}$$

Considering Eq.(11) and the fact that $e^{\mathrm{j}\phi} = e^{\mathrm{j}\Phi}$, Eq.(14) can be expanded to show the components of ϕ,

$$\widehat{\Delta S}_{\mathrm{w}} = \underset{\Delta S_{\mathrm{w}}}{\mathrm{argmax}} \left| \left\langle e^{j\left(\langle \Delta S \rangle\tilde{\xi} + \langle \xi \rangle\tilde{\Delta S} + \tilde{\xi}\tilde{\Delta S} - \langle\tilde{\xi}\tilde{\Delta S}\rangle + \Phi_e - \Delta S_{\mathrm{w}}\tilde{\xi}\right)} \right\rangle \right|. \tag{15}$$

In the case where $\Phi_e = 0$ and $\tilde{\Delta S} = 0$, this yields an unbiased estimate, i.e., $\widehat{\Delta S}_{\mathrm{w}} = \langle \Delta S \rangle$, otherwise the $\langle \xi \rangle\tilde{\Delta S}$, $\tilde{\xi}\tilde{\Delta S}$ and
240 $\left\langle \tilde{\xi}\tilde{\Delta S} \right\rangle$ terms in Eq.(15) will bias $\widehat{\Delta S}_{\mathrm{w}}$.

Figure 6 shows an example of the SlopeVar estimator being applied to a 1 km square (ground range × azimuth) window for
the inset area labelled in Fig. 5. The uncorrected phase is spatially correlated with ξ over the window as seen by comparing
Figs. 6a and 6b and by examining the 2D-histogram in Fig. 6d. Figure 6e shows the periodogram with distinct peak at ΔSWE
of 28 mm. Figure 6c shows the effect of removing the dry-snow phase component assuming constant ΔSWE of 28 mm under
245 the window which results in a much more uniform phase although residual variations can still be seen.
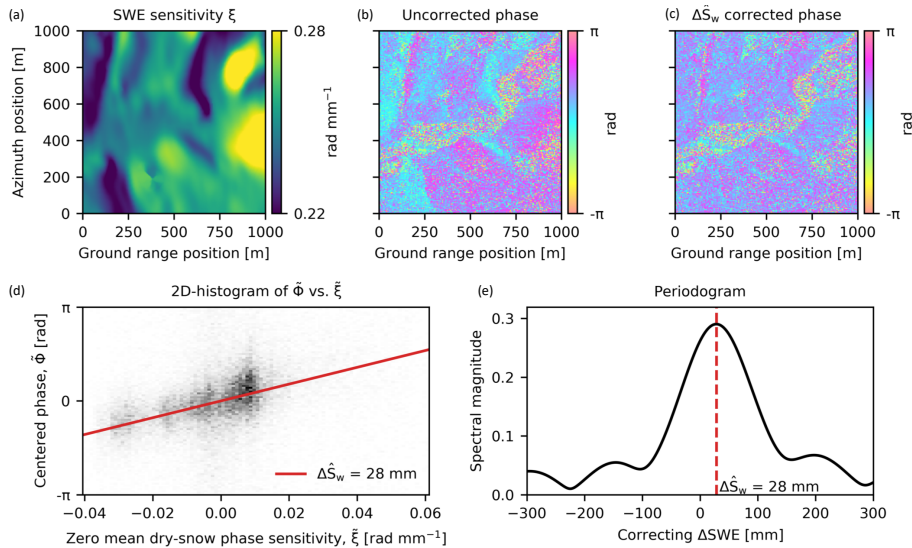
Figure 6. Example of SlopeVar ΔSWE estimation over a 1 km × 1 km window corresponding to the inset area shown in Fig. 5 for the
20120317_2010410 interferogram. (a) SWE phase sensitivity factor, ξ; (b) and (c): uncorrected and ΔSWE-corrected interferometric phase
(using SlopeVar estimate, $\widehat{\Delta S}_{\mathrm{w}}$); (d) 2D-histogram of centered phase vs. demeaned dry-snow phase sensitivity with line corresponding to
the periodogram-based estimate, $\widehat{\Delta S}_{\mathrm{w}}$; and (e) periodogram with peak corresponding to $\widehat{\Delta S}_{\mathrm{w}}$.

4.3 Estimator Implementation

Regarding estimator implementation, input interferograms were generated by co-registering the set of RS2-SLA SLCs to a common master SLC and computing sequential topographic phase corrected 3 × 12 (range pixels × azimuth pixels) multi-looked interferograms using the GAMMA software package (GAMMA Remote Sensing AG, Switzerland). Multi-looking was performed to better match the sample spacing of the interferograms to that of the DEM derived ξ map. This improved estimator computation run-time and was seen to have negligible effect on the resulting ΔSWE estimates. All interferograms were visually inspected and those with sparse coherence, typically those spanning the spring melt and early winter periods, were discarded from further analysis.

For simplicity, we only processed sequential interferograms since these provide the best coherence during the dry-snow season. However, for distributed scatterers which predominate in natural terrain, non-sequential (e.g. 48-, 72-day, ...) interferograms are known to provide additional information that can be recovered by using a phase-linking estimator (e.g., Guarnieri and Tebaldini, 2008). This could be added to the pre-estimation InSAR processing to reduce estimation variance in the future, but was deemed unnecessary for the current application.

We found the estimator to be sensitive to errors in ξ, especially those resulting from DEM errors and interpolation artifacts. High spatial-frequency errors in the ξ map tend to bias the estimated ΔSWE magnitude towards zero (discussed in Sect. 5.5). We initially used the raw TanDEM-X DEM, which we cubic-resampled to the multi-looked SAR geometry, to compute the slope and aspect angle maps required to compute ξ. The resulting ξ map contained high frequency artifacts from the cubic interpolation as well as substantial errors due to blunders in the raw DEM. Estimator performance improved significantly after we (1) manually identified and masked local DEM blunders and interpolated over them; (2) smoothed the DEM using a 2D Gaussian filter with standard deviation of 3 DEM pixels (resulting in approximately 90 m spatial resolution) to reduce high-frequency DEM errors; and (3) computed the slope angle maps prior to resampling to the SAR geometry. Note that to compute ξ according to Eq.(4) , we computed the real permittivity of dry snow as $\epsilon(\rho) = 1 + 1.5995\rho + 1.861\rho^3$, according to Leinss et al. (2015) and for simplicity, assumed $\rho = 0.3$ for all estimates (discussed further in Sect. 5.1).

We then implemented the SlopeVar estimator described in Sect. 4.2. For each candidate value of ΔS_w, the periodogram magnitude, $\left| \left\langle e^{j\left(\phi - \Delta S_\mathrm{w}\tilde{\xi}\right)} \right\rangle \right|$ can be computed efficiently using a 2D fast Fourier transform-based rectangular smooth filter over the complex-valued interferogram, allowing for generation of spatially oversampled maps at the interferogram sample spacing instead of the much coarser estimation window size. We evaluated the periodogram over the ΔSWE range of [-50 mm, 80 mm] with an interval spacing of 2 mm. Peak locations for each spatial point were then refined by fitting a quadratic by least squares using three points centered on the maximum value found over the search grid. Solutions where the maximum was within 2 grid intervals from the edge of the search range were labeled as invalid. Figure 7a shows the resulting ΔSWE map after applying the estimator to all areas of the example interferogram depicted in Fig. 5 using a 500 m square estimation window.
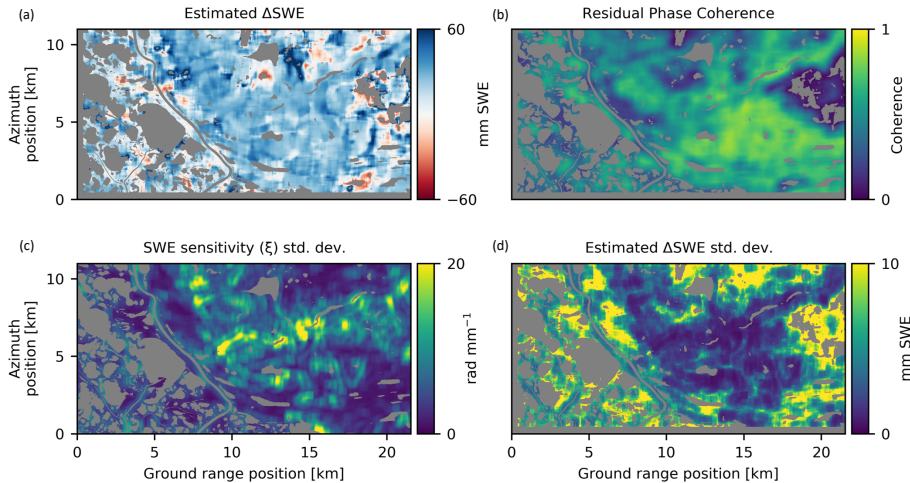
Figure 7. Example of estimated ΔSWE and ΔSWE standard deviation due to uncorrelated phase components for the 20120317_20120410 scene pair (same interferogram as shown in Figs. 5 and 6) using a window size of 500 m × 500 m. (a) estimated ΔSWE using the SlopeVar estimator; (b) coherence of residual phase after estimated dry-snow phase correction; (c) standard deviation of SWE sensitivity computed over the estimation window; and (d) Monte Carlo estimated standard deviation of estimated ΔSWE generated with ensemble of 40 simulated interferograms (see Sect. 5.4).

4.4 Precision Comparison with Delta-K ΔSWE Estimator

Our method has some similarity with the Delta-K method for estimating ΔSWE in that both methods exploit a diversity
280 in the InSAR dry-snow phase sensitivity so that absolute ΔSWE can be estimated without the need for phase unwrapping.
Furthermore, both methods operate over an estimation window, yielding results at a resolution lower than the single-look
resolution. In order to compare the two methods, we consider their relative precision estimated over a spatial window with N
multi-looked resolution-cells and assume Gaussian phase noise, which is reasonable when multi-looked interferograms with
sufficient looks are used (i.e. > 10 as noted by Hagberg et al. (1995)). Note that for the Delta-K method, multi-looking of
285 sub-band interferograms prior to computing the band-difference phases has been suggested by Bamler and Eineder (2005) to
preserve the Gaussian phase noise assumption and shown by De Zan et al. (2015) to yield better precision than the alternative
of first computing the sub-band difference and then multi-looking.

The Delta-K method exploits the phase-sensitivity diversity that exists between separate range-frequency sub-bands yielding
dry-snow phase sensitivities of $\xi \pm \Delta\xi/2$ where ξ is the sensitivity at the central carrier frequency and $\Delta\xi = B(1-b)\xi$ where
290 $B \in [0,1]$ is the normalized range bandwidth of the SAR and $b \in [0,1]$ is the sub-bandwidth fraction used. Assuming multi-
looked phase-noise with variance σ_Φ^2, the mean sub-band interferometric phase will have variance of σ_Φ^2/bN and therefore the
Delta-K difference phase will have variance $\sigma_{\Phi\_DK}^2 = 2\sigma_\Phi^2/bN$. Delta-K estimates ΔSWE according to $\widehat{\Delta S}_{DK} = \Phi_{DK}/\Delta\xi$ and
therefore the ΔSWE estimation standard deviation is,

$$\sigma_{\Delta S\_DK} = \sqrt{\frac{2}{N}} \frac{\sigma_\Phi}{B(1-b)b^{\frac{1}{2}}\xi}. \tag{16}$$

For the SlopeVar method, the estimation of ΔSWE corresponds to a linear regression over N samples and therefore, assuming $\tilde{\xi}$ is Gaussian distributed under the estimation window with variance $\left\langle \tilde{\xi}^2 \right\rangle$,

$$\sigma_{\Delta S\_SV} = \frac{\sigma_\Phi}{\sqrt{N}\left\langle \tilde{\xi}^2 \right\rangle^{1/2}}. \tag{17}$$

The relative estimation precision ratio between the two methods is therefore given by,

$$\frac{\sigma_{\Delta S\_DK}}{\sigma_{\Delta S\_SV}} = \frac{\sqrt{2}\left\langle \tilde{\xi}^2 \right\rangle^{\frac{1}{2}}}{B(1-b)b^{\frac{1}{2}}\left\langle \xi \right\rangle}, \tag{18}$$

where we have replaced ξ in Eq.(16) with the mean under the estimation window, $\langle \xi \rangle$. We use $b = 1/3$, which, neglecting system noise, is the optimum value for minimizing $\sigma_{\Delta S\_DK}$ and $B = 0.0185$ which is the normalized range bandwidth for the RADARSAT-2 Spotlight-A mode. Figure 8 shows the distribution of $\sigma_{\Delta S\_DK}/\sigma_{\Delta S\_SV}$ computed for all 500 m square estimation windows in the RS2-SLA study footprint, excluding water-bodies. The distribution has a median value of 3.8, and is > 1 for 97.5% of the area, indicating that the SlopeVar estimator can be expected to provide substantially better ΔSWE precision compared to delta-K for the great majority of areas within the study footprint.
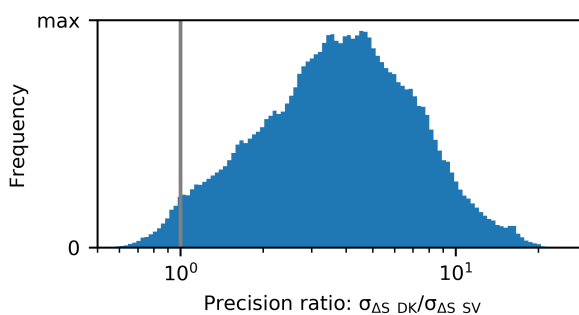
Figure 8. Histogram of the predicted ΔSWE estimation precision ratio between the Delta-K and SlopeVar methods ($\sigma_{\Delta S\_DK}/\sigma_{\Delta S\_SV}$) for all 500 m square estimation windows in the RS2-SLA study footprint. The vertical bar denotes the point of equal precision (i.e. $\sigma_{\Delta S\_DK}/\sigma_{\Delta S\_SV}$ = 1). This shows that the SlopeVar estimator provides substantially better precision for almost all areas within the study footprint.

5   Sources of Estimation Error

5.1 Snow Density Misspecification

Our proposed method relies on knowing ξ, the linear scaling factor between ΔSWE and the corresponding dry-snow phase which, as shown in Eq.(3), depends on snow density, ρ. Therefore ρ must either be known a priori or an assumed value must

310 be specified. Here we assess the effect of mis-specifying ρ. Since the method estimates ΔSWE from interferometric phase, the required density corresponds to the snowpack change rather than the actual bulk density of the snowpack, such as is the case for fresh snowfall on a dense late-season snowpack. The density of the added layer will be less than the mean density before and after the change.

A misspecification of ρ will bias the resulting ΔSWE estimate. This effect can be quantified by parameterizing ξ with respect

315 to ρ so that $\Phi_s(\rho) = \xi(\rho)\Delta S$. The fractional ΔSWE bias caused by specifying ρ' rather than the true value, ρ, is

$$\frac{\widehat{\Delta S} - \Delta S}{\Delta S} = \frac{\xi(\rho)}{\xi(\rho')} - 1. \tag{19}$$

This fractional bias is shown in Fig. 9a for true and assumed densities over the interval [0, 0.4] and it indicates that assumed densities greater or less than the true density result in a positive or negative bias, respectively. Figure 9a also shows that the bias magnitude is <5% of the true SWE change for the considered density range.
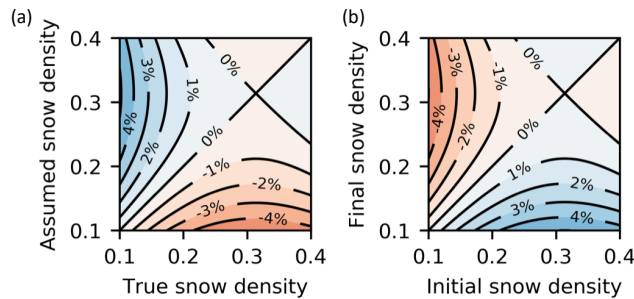
Figure 9. (a) Fractional ΔSWE estimation bias caused by misspecification of the snow density, (b) Apparent ΔSWE caused by a bulk snowpack density change in the absence of actual SWE change, as a fraction of total actual SWE.

320 In the absence of any ΔSWE, snowpack evolution may result in a bulk density change (e.g. due to settling) which will cause a snow phase contribution. This phase contribution will be spuriously attributed to a SWE change. Consider the case of a snowpack with total SWE of S that undergoes a density change from initial ρ_1 to final ρ_2. According to Eq.(5), this will cause dry-snow phase change,

$$\Phi_s = S(\xi(\rho_2) - \xi(\rho_1)). \tag{20}$$

325 Assuming that the temporal mean density of $(\rho_1 + \rho_2)/2$ is somehow known and used for estimation, the resulting ΔSWE error, S_e as a fraction of total SWE will be

$$\frac{S_e}{S} = 2\frac{\xi(\rho_2) - \xi(\rho_1)}{\xi(\rho_1) + \xi(\rho_2)}. \tag{21}$$

This fractional error is shown in Fig. 9b for initial and final densities over the interval [0, 0.4]. This shows that a density increase or decrease will respectively cause a negative or positive ΔSWE error. Since snowpack evolution generally results in

330   densification, this effect will tend to negatively bias estimated ΔSWE. However, for the considered density range, the bias is <5% of the total SWE.

For simplicity we assumed a fixed snow density of $\rho = 0.3$ for all ΔSWE estimates. This value is likely too large for the early snow-season in Inuvik and, according to Fig. 9a, likely contributes a small positive estimation bias of 1-3% to the results presented in Sect. 6. This bias could be mostly mitigated by assuming a more appropriate density according to the location and

335   time of year (e.g., Sturm and Wagner, 2010).

5.2   Violation of ΔSWE Horizontal Homogeneity Assumption

Temporal changes in SWE can be caused by a number of different processes including deposition of new snow, redistribution by wind, melt, and sublimation. Each of these processes is spatially modulated in natural terrain by the configuration of topography and vegetation (Morse et al., 2012; Anderton et al., 2004; Palmer et al., 2012). Furthermore, vegetation distribution

340   is itself modulated by topography (Walker, 2000). For these reasons, spatial variation of ΔSWE over a particular time period is likely to show some correlation with topography; either directly with elevation or with derived indices such as slope, aspect or measures of curvature.

As shown in Sect. 4.1, the estimation of ΔSWE within a spatial window through the correlation with the topographic variation of dry-SWE phase sensitivity $\tilde{\xi}$, is subject to bias when there are horizontal ΔSWE variations within the window that

345   are correlated with either $\tilde{\xi}$ itself or with $\tilde{\xi}^2$. To investigate the significance of this effect, we simulated the seasonal evolution of spatially variable ΔSWE distributions due to variations in topography and vegetation using SnowModel (Liston and Elder, 2006), implemented as a Fortran software package that includes sub-models for metrological forcing conditions, surface energy exchanges, snowpack evolution, and 3D wind transport. We simulated an evolving snowpack over several snow seasons for two cases: (1) bare-earth case with no snow-holding vegetation to examine the impact of topographic variation only; and

350   (2) spatially variable vegetation heights (i.e. variable snow-holding capacity) to consider the additional influence of vegetation. The spatially varying vegetation was modeled using the NALCMS 2015 land-classification data for our study area.

We chose a study area and time period for the simulation that correspond to the spatial footprint and a similar time period as the RS2-SLA dataset we used for the method demonstration described in Sect. 2. SnowModel also takes as input the digital elevation model of the study area and one or more time series of meteorological driving data in the form of regularly sampled

355   temperature, wind and precipitation data. We ran the model using the same TanDEM-X DEM used for InSAR topographic phase correction and SWE change estimation, and meteorological forcing data from three locations: (1) Environment Canada (EC) Inuvik Climate station [68.32° N, -133.53° E], adjacent to position 'E' in Fig. 1a (ECCC, 2021b); (2) EC Trail Valley Creek station [68.74° N, -133.50° E], 43 km north of the scene center; and (3) the Government of Northwest Territories -

Environment and Natural Resources (GNWT-ENR) Southern ITH station [68.54° N, -133.77° E], 21 km north of the scene

360   center (dataset provided directly from GNWT-ENR). The model was run with default settings at a daily-step time interval with results output every 24-days corresponding to the imaged dates of the RS2-SLA dataset. The resulting absolute SWE maps, produced in the original DEM spatial reference were resampled to the RS2-SLA range-Doppler geometry and sequentially differenced to produce 24-day ΔSWE maps.

These ΔSWE maps were then used along with the dry-snow phase sensitivity ξ map, computed from the DEM with a
365   nominal relative snow density of $\rho = 0.3$, to determine the expected ΔSWE estimation error according to the first two terms in Eq.(13) , i.e. those related to the spatial variation of ΔSWE, $\tilde{\Delta S}$). The modelled ΔSWE error maps were computed with rectangular estimation windows with 500 m × 500 m ground footprint.

We analyzed our simulations for all 24-day intervals from 2011-07-17 to 2020-04-29 falling within the expected dry-snow season, nominally chosen to be Oct. 1 to Mar 31 of each year based on the climate normals for Inuvik (see Fig. 2). The
370   results, summarized in Fig. 10, show the spatial distribution of the ΔSWE error averaged over all modelled time intervals and histograms of all expected ΔSWE errors and the per-interval spatially averaged mean ΔSWE error.
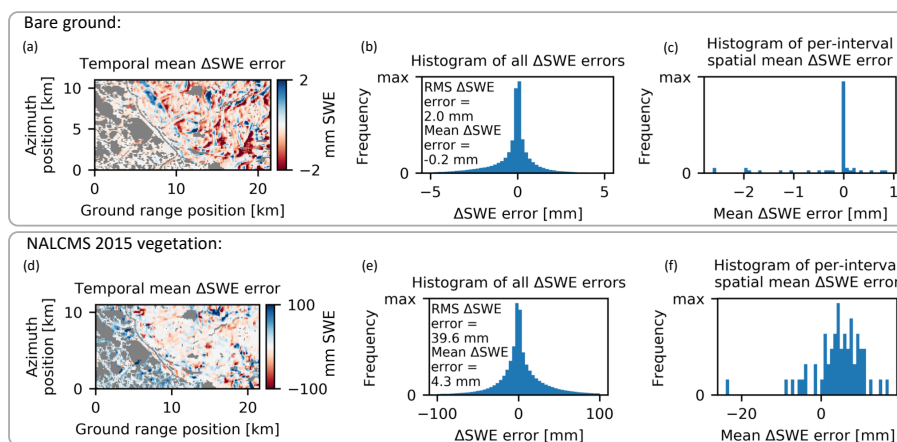
Figure 10. Results for ΔSWE simulation for the bare-ground (top row) and NALCMS 2015 vegetation distribution (bottom row) cases for the RS2-SLA geometry over Inuvik for the period 2011-07-17 to 2020-04-29. Sequential 24-day ΔSWE were simulated for the dry-snow season each year (nominally chosen to be Oct 1 to Mar 31 according to Fig. 2) resulting in a total of 60 24-day intervals being simulated. (a) and (d) temporal mean of the expected ΔSWE error; (b) and (e) histogram of all expected errors (all spatial estimates over all time intervals); (c) and (f) histogram of the spatial mean ΔSWE error for the set of intervals.

For the bare earth case (Figs. 10a, 10b and 10c), a single outlier interval (2012-01-05 to 2012-01-29) was omitted from the summary analysis because the errors for that interval were very large compared to all other intervals. This appears to be due to a strong correlation of the simulated spatial ΔSWE distribution with $\tilde{\xi}$ for that 24-day interval which can occur when a
375   strong wind-transport event directionally aligns with the horizontal projection of the SAR line-of-sight. Hence, the simulated topography modulated scouring and deposition along the wind-direction axis can, by chance, align with the SAR geometry

ground-range direction which results in a very large estimation bias. It may be possible to detect these events by analysis of the wind history (e.g. thresholding of a suitable blown-snow index while also considering the wind direction with respect to the SAR ground-range direction). We investigated this approach by computing the time varying blowing snow probability as

380 modelled by Li and Pomeroy (1997) which provides the probability that blowing snow conditions will occur as a function of wind speed and temperature. We computed these at daily time-steps, assigned the mean wind-direction to each time step and then integrated these 2D vectors over the 24-day simulation intervals. The result is a directional cumulative blowing snow index in units of hours (of blowing snow) and is shown in Fig. 11 for all simulated 24-day intervals. This shows that the SnowModel outlier case is also an outlier with respect to the blowing snow index magnitude (and also when projected to the SAR look

385 direction axis) suggesting that wind-driven redistribution is responsible for the predicted large ΔSWE bias.
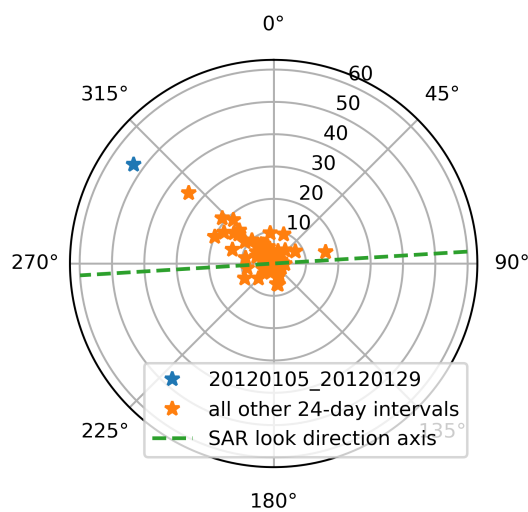
Figure 11. Directional cumulative blowing snow hours computed using ERA-5 surface parameters applied to the Li and Pomeroy (1997) probability model for all simulated 24-day intervals. The 20120105_20120129 interval appears as an outlier with respect to the cumulative magnitude. The SAR look direction axis is shown for comparison.

For the bare ground case, the temporal mean ΔSWE error map shows mean errors in the +/- 2 mm range with a spatial pattern that is correlated with the topography (Fig. 10a). The distribution of all ΔSWE errors (Fig. 10b), has a mean of just -0.2 mm which corresponds to a small negative overall estimation bias and an RMS value of 2.0 mm which corresponds to approximately 20% of the simulated mean per-interval ΔSWE change. The histograms of the per-interval spatially averaged

390 errors (Fig. 10c) show that the majority of 24-day intervals have a mean error near zero, suggesting that averaging estimates over wider areas reduces the bias effect introduced by spatially variable ΔSWE distribution.

For the NALCMS 2015 vegetation case, the temporal mean ΔSWE error map (Fig. 10d) shows mean errors with magnitudes that are much larger than for the bare earth case (up to 100 mm in some areas) corresponding to areas with heterogenous vegetation classifications (see Fig. 1c). The distribution of ΔSWE errors (Figs. 10e and 10f), has a mean and RMS value of

395 4.3 mm and 39.6 mm which are very substantial. This suggests that spatially varying vegetation snow holding conditions may substantially bias the ΔSWE estimates. However, it should be noted that results from real data, presented in Sect. 6, do not show such large variations as would be expected by the error magnitudes in Figs. 10d, 10e and 10f. The reason could be that the simulation driven by the NALCMS vegetation classification significantly over-represents the effect of spatially variable vegetation. Nevertheless, these results highlight the relative importance of vegetation as a source of method bias and suggest

400 that some form of mitigation may be required to yield useful estimates from the proposed method in areas with variable vegetation snow-holding heights.

We compared the relative contributions of the $\langle \xi \rangle \left\langle \tilde{\xi} \tilde{\Delta S} \right\rangle$ and $\left\langle \tilde{\xi}^2 \tilde{\Delta S} \right\rangle$ contributions to the ΔSWE error which showed that for all 24-day intervals, and both bare earth and NALCMS 2015 cases the RMS of the $\langle \xi \rangle \left\langle \tilde{\xi} \tilde{\Delta S} \right\rangle$ component was much greater than that of the $\left\langle \tilde{\xi}^2 \tilde{\Delta S} \right\rangle$ component so that with respect to the influence of $\tilde{\Delta S}$, the spatial correlation with respect to

405 $\tilde{\xi}^2$ can be neglected.

5.3 Correlated Phase Components

As shown in Eq.(12) , additional phase components, other than dry-snow refractive phase, will contribute to ΔSWE estimation error according to their spatial correlation with the dry-snow phase sensitivity: $\left\langle \tilde{\xi} \Phi_e \right\rangle / \left\langle \tilde{\xi}^2 \right\rangle$. We distinguish between (1) systematic spatial correlation between the dry-snow phase sensitivity and additional phase components that have a topographic

410 dependence and (2) spurious correlations with phase components that are not systematically dependent on topography due to sampling statistics over the finite estimation window. In this section we consider the former by examining several phase components, their spatial characteristics with respect to topographic slope and their expected contribution to ΔSWE estimation error. Uncorrelated phase components are discussed in Sect. 5.4.

5.3.1 Atmospheric delay

415 The troposphere contributes substantial phase delay during SAR imaging (Hanssen, 2001). This delay can be decomposed into a horizontal mean component and a horizontally variable component which we respectively denote as the 'static' and 'dynamic' components. Temporal differences in the static component between image acquisitions results in a phase component that is modulated by topography. Neglecting any height dependence of the delay over the height range within the estimation window, the phase can be modelled as a simple linear function (Lin et al., 2010),

420 $$\Phi_{\mathrm{sa}} = \frac{4\pi}{\lambda} \Delta K h + \beta, \tag{22}$$

where ΔK is the linear transfer function coefficient corresponding to the volumetric mean delay difference between SAR acquisitions, h is the topographic height and β is an offset constant which we set to zero without loss of generality since we consider only the correlation of Φ_{sa} with zero-mean $\tilde{\xi}$. Note that the horizontal variation of ΔK is gradual and therefore ΔK can be assumed constant within the estimation window. Therefore, the spatial variation of Φ_{sa} within the ΔSWE window

425 (assumed to be ≤ 1 km) can be attributed solely to topographic height variation.

The dynamic component is driven by turbulent mixing and therefore its spatial power spectrum follows a power-law relationship, which limits the amplitude at spatial scales below a few km (Hanssen, 2001). Therefore, for estimation windows <1 km, the dynamic component can reasonably be neglected. For larger estimation windows (not explicitly considered in this paper), the influence of the dynamic component can be mitigated by spatial high-pass filtering both the InSAR phase as well

430 as ξ prior to ΔSWE estimation, similar to the method employed by Lin et al. (2010) for estimating ΔK from interferograms.

Figures 12a and 12d show the expected ΔSWE estimation error for the case of $\Delta K = 10^{-5}$ (i.e. 10 mm km^{-1}). For this case the RMS error is 1.1 mm SWE. However, the distribution is centered around zero so that the mean error is only 0.04 mm SWE. Therefore, spatial averaging of the estimates over a sufficient area will tend to mitigate the error due to static atmospheric delay.
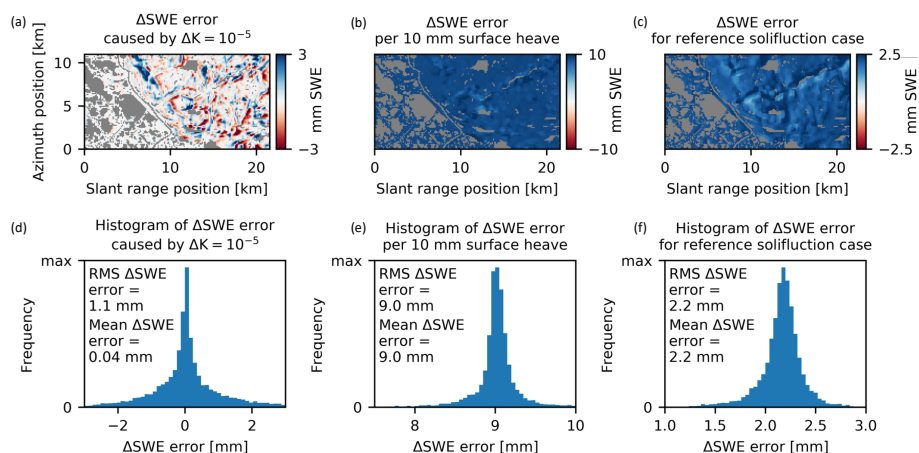
Figure 12. Expected contribution of topographically correlated phase components to ΔSWE estimation error. (a) and (d) show the error due to a static atmospheric volumetric delay error of $\Delta K = 10^{-5}$; (b) and (e) show the error per 10 mm of surface heave over the time interval; (c) and (f) show the error for reference solifluction case ($V_{\text{sf}} = 37$ mm y$^{-1} \cdot \tan\alpha$, corresponding to surface velocity of 10 mm y^{-1} for a slope of $\alpha = 15°$, evaluated for a 24 day interval).

Regarding the temporal distribution of ΔK, given that it is a pairwise differential quantity, it has zero expectation on an

435 annualized time-scale. However, there is some seasonal dependence on tropospheric delay (Cong et al., 2012) and therefore ΔK, for sequential dry-snow season interferograms, should not be considered temporally random. For a particular spatial location, the errors may accumulate constructively over a snow season to yield a consistent, albeit small, bias effect for that location. However, methods exist for the estimation of ΔK either by correlation with topographic height over estimation windows corresponding to the full-scene or tens of kilometers (Lin et al., 2010; Bekaert et al., 2015), or from climate reanalysis

440 data (Cong et al., 2012). Therefore, interference by static atmospheric phase is not considered a limiting factor for the proposed method, since the effect can be largely mitigated.

5.3.2 Surface displacement

Surface displacements may result from freezing that causes upward heave and thawing that causes downward subsidence, either near the surface in soil layers that freeze and thaw seasonally or deeper in the case of permafrost aggradation or degradation in

445 periglacial regions. Surface displacements associated with freezing or thawing are predominantly in the direction of the local surface normal and therefore spatial variation of the InSAR phase signal induced by such displacement is approximated by

$$\Phi_{\mathrm{he}} = -\frac{4\pi}{\lambda} d_h \cos\theta, \tag{23}$$

where d_h is the displacement magnitude away from the reference surface, with positive and negative displacements respectively corresponding to freezing (heave) and thawing (subsidence).

450   In equilibrium climate conditions, seasonal active-layer displacement tends to follow a pattern of heave in early- to mid-winter related to freeze-back to the top of permafrost, which is followed by static conditions until the spring when air temperatures rise above 0 °C. Then the active layer thaws continually throughout the summer with gradual subsidence until the mean daily surface temperature remain below 0 °C again. Therefore, the dry-snow season can be divided into an initial period of positively valued displacement followed by a static period. Longer-term positively or negatively valued displacement may

455 be superimposed onto this seasonal pattern due to changes in permafrost conditions such as ground ice loss (subsidence) due to climatic warming trends or surface disturbance that cause permafrost degradation, or ground ice gain (heave) due to climatic cooling trends or changing surface conditions that cause permafrost aggradation. Annual displacement amplitudes for seasonally frozen terrain typically occur in the range of 20 to 120 mm (Gruber, 2020), and are normally greater in fine-grained, frost-susceptible soils (e.g., morainal deposits with a high silt content), and lesser in coarse-grained non frost-susceptible soils

460 (e.g., glaciofluvial deposits with a high sand content).

    To assess the significance of heave as an interfering factor we consider a reference case where d_h= 10 mm over a 24-day interval. Figures 12b and 12e show the expected ΔSWE estimation error for this reference case. The error is always positively valued and corresponds to an approximately +9 mm ΔSWE bias over the 24-day estimation interval which is very substantial. Hence, there is potential for displacement processes, if present, to significantly interfere with the proposed estimation method.

465   One mitigation approach is to limit use of the estimator spatially and temporally to correspond to known areas and periods of low displacement activity. For example, temporal analysis of summer interferograms can be used to identify areas with significant subsidence and these can be masked out during ΔSWE estimation under the assumption that thaw-period subsidence is spatially correlated with freeze-period heave. Of course, this is not possible for the case of widespread seasonal surface displacement as is common in periglacial regions.

470 5.3.3 Solifluction

We consider slow moving, gravity-driven surface soil flux, i.e., solifluction, as a potential interfering phase component since it is correlated with topographic slope. We do not expect solifluction to be a significant bias source during the dry-snow season but include it because it may affect snow-free interferograms analyzed for the purpose of method validation.

Solifluction is driven by cyclical surface displacement (diurnal or seasonal) coupled with sufficient topographic slope mag-
475 nitude and environmental conditions that include vegetation type, soil moisture content, and soil grain-size distribution (Mat-
suoka, 2001), and it is common in periglacial regions. The flow direction is principally in the local downslope direction and
therefore the resulting InSAR phase is approximated by

$$\Phi_{\mathrm{sf}} = \frac{4\pi}{\lambda} V_{\mathrm{sf}} \Delta t \left(\widehat{\mathbf{L}} \cdot \widehat{\mathbf{D}} \right),$$ (24)

where V_{sf} is the surface velocity magnitude due to solifluction, Δt is the InSAR pair temporal baseline, and $\widehat{\mathbf{L}}$ and $\widehat{\mathbf{D}}$ are
480 the unit magnitude SAR look and downslope direction vectors. Assuming homogenous soil conditions within the estimation
window, spatial variation of V_{sf} can be modelled as a function of topographic slope angle only. A commonly applied model is
given by Matsuoka (2001),

$$V_{\mathrm{sf}} = \beta_{\mathrm{sf}} \tan \alpha,$$ (25)

where β_{sf} is a scaling factor, which we assume is constant over the window. In order to assess the significance of solifluction as
485 an interfering factor we consider a reference case where $V_{\mathrm{sf}} = 10$ mm y^{-1} for a slope of $\alpha = 15°$. This corresponds to $\beta_{\mathrm{sf}} = 37$
mm y^{-1}. Figures 12c and 12f show the expected ΔSWE estimation error for this reference case. The error is always positively
valued and corresponds to a 2.2 mm SWE bias for a 24-day estimation interval.

It is noteworthy that both the heave (upward normal-to-surface) and solifluction (downward tangential-to-surface) result in
positively valued biases. In the case of symmetric surface displacement (heave followed by equal magnitude subsidence along
490 surface normal – so called 'retrograde' motion) the net ΔSWE bias over the cyclical period (including snow-free thaw-season
interferograms) is zero. However in the more general case of heave followed by a combination of retrograde motion and
solifluction, e.g. as demonstrated by Harris et al. (2008), the result is net positive ΔSWE bias.

5.3.4 Soil Moisture

Near surface soil moisture conditions are a known contributor to the InSAR phase signal (Nolan et al., 2003) and these are
495 likely modulated by topographic slope both in terms of gravity-driven effects on near surface hydrology and the influence of
slope aspect on solar heating. As such, there may be some correlation with the dry-snow phase sensitivity leading to estimation
bias. As with solifluction, we do not expect soil moisture to significantly affect dry-snow interferograms but consider its effect
on snow-free interferograms used as method validation controls.

Although the correlation of soil moisture phase with topographic slope is difficult to model, it is possible to establish a bound
500 on its impact on the ΔSWE estimation by considering that the soil moisture phase magnitude, Φ_{sm} is limited to some maximum
value, $\Phi_{\mathrm{sm\_max}}$ according to sensor wavelength and soil type (De Zan et al., 2014). Considering a case where $\xi \in [\xi_{\min}, \xi_{\max}]$,
the spatial distribution of Φ_{sm} producing maximum possible ΔSWE estimation bias is

$$\Phi_{\text{sm}} = \Phi_{\text{sm\_max}} \frac{\xi - \xi_{\text{min}}}{\xi_{\text{max}} - \xi_{\text{min}}} \tag{26}$$

which corresponds to perfect correlation between Φ_{sm} and ξ. According to Eq.(12) this yields a ΔSWE bias limit of $\Phi_{\text{sm\_max}}/(\xi_{\text{max}} -$

505 $\xi_{\text{min}})$. Considering our study case, $\xi \in [0.22 \text{ rad mm}^{-1}, 0.28 \text{ rad mm}^{-1}]$ (see Fig. 5a) and assuming $\Phi_{\text{sm\_max}} = 90°$, which is reasonable considering the model of De Zan et al. (2014) and the simulation results from Rabus et al. (2010), this corresponds to a bias magnitude limit of 1.3 mm SWE which is relatively small especially when considering that any actual spatial correlation is likely much less than this ideal upper limit.

5.4 Uncorrelated Phase Components

510 Phase components not systematically correlated with $\tilde{\xi}$ will contribute to the ΔSWE estimation error due to finite-sampling over the estimation window. These include decorrelation phase noise and the non-$\tilde{\xi}$ correlated parts of the components described previously in Sect. 5.3. In the case of these spurious correlations, the resulting estimation error magnitude can be expected to diminish with larger estimation window sizes and, in the global sense, will not systematically bias the estimates but instead contribute to the variance.

515 Decorrelation occurs in repeat-pass InSAR because of spatial differences in the imaging geometry, temporal changes in the scattering environment including snow wetting/melt and system effects including thermal noise and SAR processing errors (Zebker and Villasenor, 1992). Furthermore, we expect some dependence of decorrelation on the true ΔSWE magnitude due to variations in the refractive dry-snow phase at both the sub-resolution scale and at the sub-estimation window scale. The contributions include those due to horizontal snow depth variations caused either by varying ground surface heights as

520 described by Rott et al. (2003) and especially in the early snow-season when short scale undulations 'fill-in', and spatial depth variations due to snow surface structure at scales larger than the radar wavelength.

The amount of decorrelation can vary significantly both spatially within each interferogram and temporally depending on changing surface conditions and pass-to-pass variations in the SAR orbit. It is therefore important to estimate the ΔSWE variance contribution as a space and time varying quantity.

525 Specifying the transfer function between phase noise and ΔSWE estimation variance is made difficult by the fact that the distribution of $\tilde{\xi}$ is generally unique for each estimation window. We decided to apply the Monte Carlo approach by simulating a sufficiently large ensemble of zero-signal partially decorrelated interferograms, applying the ΔSWE estimation on each instance and then computing statistics over the ensemble of estimates. This requires knowledge of the space and time varying uncorrelated phase error distribution. We approximate this as the distribution of a circular complex stationary white process

530 with zero mean phase as described by Just and Bamler (1994) and which is uniquely specified by the coherence magnitude, γ. We estimate γ as the ensemble coherence of the residual phase after removing the dry-snow phase components using the ΔSWE estimate,

$$\widehat{\gamma} = \left| \left\langle e^{j\left(\phi - \widehat{\Delta S}\xi\right)} \right\rangle \right|. \tag{27}$$

As such, this approach can be used to estimate a unique ΔSWE estimation variance map for each source interferogram.

535 Figures 7b, 7c and 7d respectively show the residual phase coherence map, the standard deviation of SWE sensitivity under the window (i.e. $\left\langle \tilde{\xi}^2 \right\rangle^{1/2}$) and the resulting Monte Carlo-based error estimation for the same interferogram depicted in Fig. 5. Local factors affecting the estimated ΔSWE variance include: (1) the residual coherence magnitude; (2) the diversity of ξ within the estimation window; and (3) the spatial support under the window (areas adjacent to water bodies have a smaller ensemble of valid phase samples and hence a larger variance).

540 ## 5.5 DEM Error

Errors in the DEM used for analysis contribute to the ΔSWE estimation error due to both residual topographic phase (as a component of total phase error, Φ_e) and error in the DEM-derived phase-sensitivity, $\tilde{\xi}$, used by the estimator.

The topographic phase error scales linearly with both perpendicular orbit baseline, $B_\perp$, and DEM error, Δh,

$$\Phi_{\text{topo}} = \frac{4\pi}{\lambda} \frac{B_\perp \Delta h}{R \sin\theta}. \tag{28}$$

545 Considering the Φ_e term in Eq.(13) and the fact that Δh varies spatially, the resulting ΔSWE bias scales with $B_\perp E\left(\left\langle \tilde{\xi}\Delta h\right\rangle\right)$ for a single interferogram and with $E\left(B_\perp\right)E\left(\left\langle \tilde{\xi}\Delta h\right\rangle\right)$ with respect to all interferograms. We assume that $E\left(B_\perp\right)$ is zero for a sensor with a maintained orbit and therefore this effect is likely unbiased with respect to a temporal set of ΔSWE maps. Furthermore, the effect can also be neglected if one assumes that that Δh is uncorrelated with $\tilde{\xi}$, which may or may not be the case depending on the DEM used.

550 Next, we consider the effect of errors in $\tilde{\xi}$ caused by DEM errors. The estimator defined in Eq.(12) can be better expressed using the DEM derived dry-snow phase sensitivity, $\tilde{\xi}_D = \tilde{\xi} + \tilde{\xi}_{\Delta h}$, instead of true $\tilde{\xi}$ where $\tilde{\xi}_{\Delta h}$ is the error in $\tilde{\xi}_D$. Furthermore, for simplicity we assume that homogenous dry-snow change is the dominant phase contribution such that $\tilde{\Phi} \cong \langle \Delta S\rangle \tilde{\xi}$. Therefore,

$$\widehat{\Delta S} = \frac{\left\langle \tilde{\xi}_D \tilde{\Phi}\right\rangle}{\left\langle \tilde{\xi}_D^2\right\rangle} \cong \langle \Delta S\rangle \left(\frac{\left\langle \tilde{\xi}^2\right\rangle + \left\langle \tilde{\xi}\tilde{\xi}_{\Delta h}\right\rangle}{\left\langle \tilde{\xi}^2\right\rangle + \left\langle \tilde{\xi}_{\Delta h}^2\right\rangle + 2\left\langle \tilde{\xi}\tilde{\xi}_{\Delta h}\right\rangle}\right). \tag{29}$$

555 If we assume that $\tilde{\xi}_{\Delta h}$ is uncorrelated with $\tilde{\xi}$,

$$\widehat{\Delta S} \cong \langle \Delta S\rangle \left(1 - \frac{\left\langle \tilde{\xi}_{\Delta h}^2\right\rangle}{\left\langle \tilde{\xi}^2\right\rangle + \left\langle \tilde{\xi}_{\Delta h}^2\right\rangle}\right). \tag{30}$$

which corresponds to a multiplicative bias towards lower amplitudes that is more pronounced in areas with low ξ diversity, i.e. low $\left\langle \tilde{\xi}^2\right\rangle$. We have not attempted to quantify $\left\langle \tilde{\xi}_{\Delta h}^2\right\rangle$ for our TanDEM-X DEM derived ξ map but we made efforts to reduce it by smoothing the DEM (see Sect. 4.3), noting that this approach has its limits since over-smoothing will tend to increase
560 $\left\langle \tilde{\xi}_{\Delta h}^2\right\rangle$.

6 Results and Discussion

6.1 ΔSWE Estimation Maps

We computed 95 coherent sequential interferograms from the assembled set of 120 RS2-SLA SLCs and these were used with the SlopeVar estimator to generate ΔSWE estimation maps using an estimation window of 500 m × 500 m (ground range ×

565   azimuth). This corresponds to 46 snow-season interferograms over 2 partial and 8 complete snow-seasons and 49 non-snow interferograms over 9 snow-free seasons. The estimator was run on the snow-free season interferograms to serve as control cases since these are known to have zero dry-snow ΔSWE. Additionally, the Monte Carlo-based variance estimator described in Sect. 5.4 was run on all interferograms. Water bodies and areas with no valid solution from the periodogram peak-finding analysis were labelled as invalid and masked out. Figure 13 shows an example set of five such ΔSWE maps from the 2017-2018

570   snow-season (all snow-season ΔSWE maps from the 2012-2021 dataset are shown in Fig. S1).
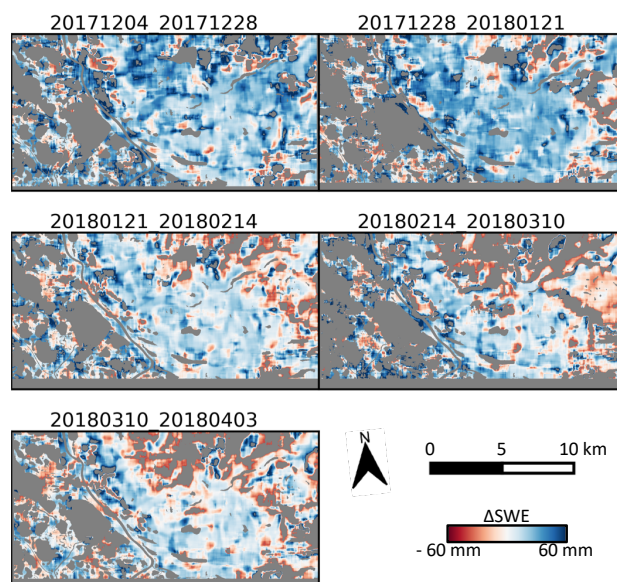
Figure 13. Dry-snow season ΔSWE maps from the 2017-2018 snow-season, estimated with the SlopeVar estimator. Water areas and points with no solution in the ΔSWE search range are greyed out. Date pairs are formatted as yyyymmdd_yyyymmdd.

6.2 Comparison of ΔSWE Estimates with In Situ Measurements

In order to verify the ΔSWE estimates we compiled a number of mid-to-late winter snow transect surveys that are summarized in and their positions A-E are labelled in Fig. 1a. These surveys are comprised by: 1) three transects at sites A, B and C that are immediately north of Inuvik, all surveyed by the authors on the same day; (2) one transect, located at site D, provided by

575   Tim Ensom (Wilfred Laurier University) in a fully tree-covered area adjacent to a small creek; and (3) a series of four transect

measurements made at the same location, site E, by GNWT-ENR at two-week intervals at a site with mixed trees and shrubs that is adjacent to the Inuvik Satellite Station Facility.

To compare with these absolute SWE measurements, we generated snow season cumulative SWE maps by integrating the sequential SlopeVar estimated ΔSWE maps through time; starting with the first dry-snow interferogram identified for each
580   snow season. As discussed in Sect. 4.3, some ΔSWE estimates are labelled as invalid due to lack of a distinct periodogram peak. On average these correspond to about 10% of non-water spatial samples and therefore, in order to preserve temporal continuity for the integration, these were replaced with values obtained by smoothing all valid estimates within a 2 km square window. The cumulative SWE maps do not represent estimates of true absolute SWE because early snow-season interferograms are generally not sufficiently coherent to allow ΔSWE estimation and therefore some amount of accumulated SWE is not
585   accounted for. Therefore, for the comparison, the in situ measurements correspond to an upper-limit for the SlopeVar estimated total SWE maps.

We also estimated variances for the cumulative SWE maps by summing the Monte Carlo derived per-interval variance estimates, assuming they are uncorrelated through time.

For each transect dataset, all SWE measurements were averaged to generate a mean value for the local area and the sample
590   standard deviation was used to compute a corresponding standard error. The in situ measurements were each made on a particular date, whereas the InSAR cumulative SWE maps are produced at 24-day intervals. The cumulative SWE maps temporally bracketing each transect date were therefore sampled at the spatial mean position of the transect and then linearly interpolated in time to generate a cumulative SWE estimate for that point in space and time. Likewise, the error variance maps were also interpolated and converted to standard-deviations.

595   Figure 14 shows a scatterplot comparison of the InSAR derived cumulative SWE estimates and the transect mean SWE values. Vertical and horizontal error bars correspond to one standard-deviation and one standard-error respectively. Seven of the eight transects are within one standard deviation of the 1:1 line, and demonstrate good agreement between the measured and estimated values. Treating the transect mean values as truth, and neglecting the unaccounted early snow-season SWE, the RMSE for all transect comparisons is 15 mm. It is noteworthy that the author-surveyed transects (locations 'A', 'B', and 'C')
600   correspond to areas of low topographic variation as indicated by the rightmost column of Table 2, and, as shown in Fig. 14, (locations 'A', 'C') have larger predicted total SWE standard deviations (i.e. >25 mm). This is consistent with the fact that estimation variance is expected to increase with decreasing ξ diversity.

6.3 Comparison of ΔSWE Estimates with Predicted Temporal Change

The estimator results were examined temporally by comparing the spatial mean of each estimated ΔSWE map, after projection
605   to ground range geometry, with the corresponding SWE change predicted by the European Centre for Medium-Range Weather Forecasts (ECMWF) ERA5 reanalysis model (Hersbach et al., 2020) over the same time interval. We chose ERA5 for comparison based on Mortimer et al. (2020) who report that it compares favourably to independent snow course data, and more so than currently available global passive microwave products do. The gridded ERA5 results were spatially interpolated to the RS2-SLA scene center. Note that all but five of the analyzed interferograms span 24-day intervals. The additional five intervals

Table 2. List of transect snow surveys used for in situ comparison with SlopeVar results.

Source	Date (yyyy-mm-dd)	Site	Position (Lat., Long.)	Length (m)	Sample size (n)	Snow sampler (Model diameter in cm)	$\langle \tilde{\xi}^2 \rangle^{1/2}$ [a] (radians·mm^{-1})
Authors of this paper	2018-03-15	A	68.398° N, -133.775° E	200	21	Metric Prairie Snow Sampler (6)	2.5
	2018-03-15	B	68.375° N, -133.733° E	140	15		2.3
	2018-03-15	C	68.380° N, -133.740° E	100	11		1.0
Tim Ensom	2018-04-22	D	68.316° N, -133.517° E	124	21	ESC-30 (6)	12.8
GNWT-ENR	2017-02-01	E	68.319° N, -133.532° E	Not reported	10	Metric Prairie Snow Sampler (6)	5.9
	2017-02-15				10		
	2017-03-01				10		
	2017-03-16				10		

[a] Standard deviation of dry-snow phase sensitivity factor, ξ, computed over local 500 m × 500 m estimation window.
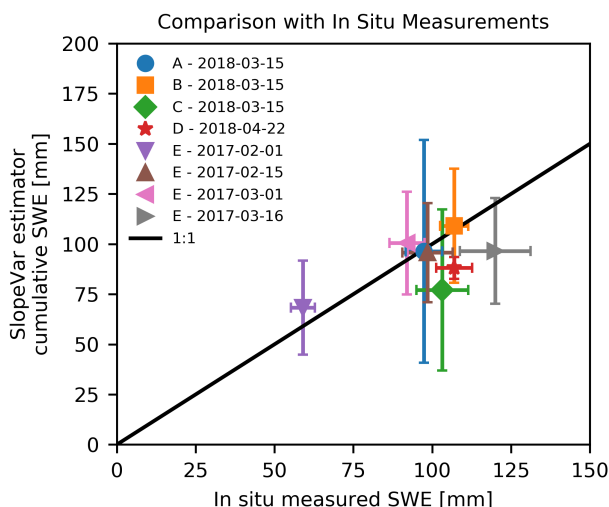
Figure 14. Comparison of SlopeVar estimator cumulative SWE with in situ snow-tube sampled SWE transect measurements. Error bars correspond to the snow season-accumulated SWE standard deviation (vertical) and the transect measurement standard error (horizontal). Labels A-E correspond to the survey locations, shown in Fig. 1a.

610   each span 48-days due to missed SAR acquisitions. For the temporal comparison, each of these five intervals were split into two 24-day intervals with half the estimated SWE change arbitrarily assigned to each interval.

Figure 15a compares the continuous ERA5 24-day interval ΔSWE history time-series with the SlopeVar estimator results. Figure 15b shows the same data as a scatter-plot comparison. Both plots are labelled according to time-of-year as four annual quarters to highlight seasonal effects. Treating the ERA5 estimates as truth, Table 3 shows error statistics (bias, RMSE and

615 correlation coefficient) for a number of temporal subsets that include the four seasonal quarters, all intervals, the nominal
dry-snow period (Oct-Mar), and the 'No snow' intervals (all intervals with zero ERA5 SWE at both interval endpoints).
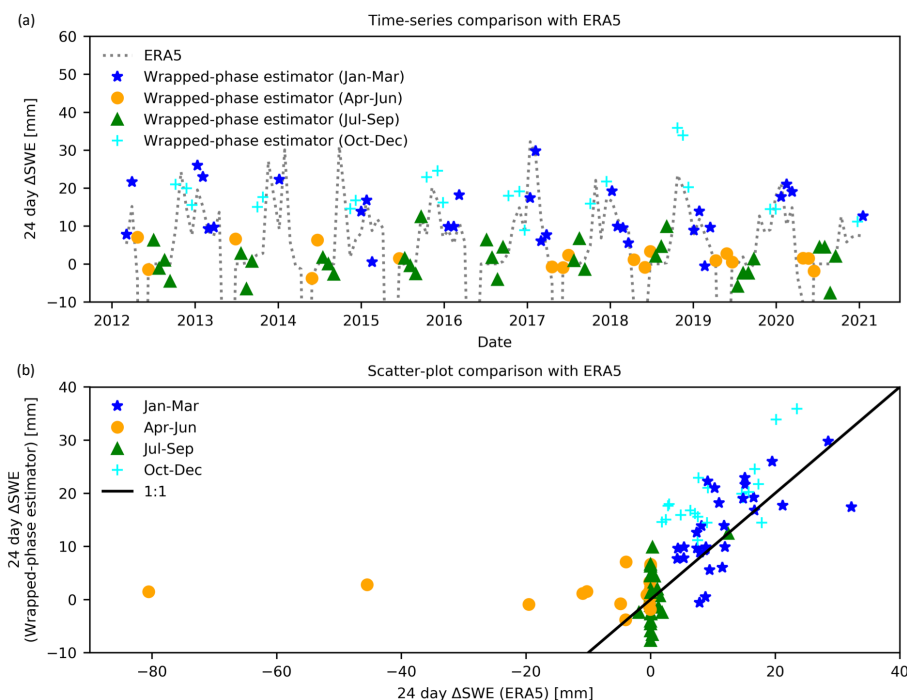
Figure 15. Time series (a) and scatterplot (b) comparisons of SlopeVar estimator 24 day interval ΔSWE with ERA5 reanalysis estimates.
SlopeVar estimator point symbols are separated according to season to illustrate the seasonal dependence of the bias (especially difference
between Oct-Dec and Jan-Mar points) apparent in the scatterplot.

Table 3. SWE error statistics for SlopeVar estimator compared to ERA5 reanalysis estimates.

Subset	Sample size (n)	Bias (mm)	RMSE (mm)	Correlation coefficient (r)
Jan-Mar	29	1.7	6.1	0.64
Apr-Jun	18	11.5	23.5	-0.01
Jul-Sep	32	0.4	4.1	0.44
Oct-Dec	21	8.6	9.9	0.69
All	100	4.5	11.7	0.56
Oct-Mar	50	4.6	7.9	0.57
No snow[a]	23	1.7	4.2	-

[a]All intervals with zero ERA5 SWE at both interval endpoints.

Regarding correspondence with ERA5, we are primarily concerned with the Oct-Dec and Jan-Mar estimates because these correspond with the dry-snow period when the estimator is expected to provide useful results. Figure 15b shows that these do follow the 1:1 correspondence line. However, the Oct-Dec points appear to have a significant positive bias whereas the Jan-Mar

620   points do not. This is quantified in Table 3, which shows that, in aggregate, the Oct-Mar time period has a correlation of 0.57 with respect to ERA5, which is moderately strong. There is an 8.6 mm per-interval ΔSWE bias for Oct-Dec but only 1.7 mm for Jan-Mar. This is consistent with the expected impact of early freeze-season heave, which, as shown in Sect. 5.3 is expected to yield a positive bias until freeze back of the active-layer completes. Considering the result from Fig. 12e where 10 mm of heave results in a mean ΔSWE bias of 9 mm, the Oct-Dec bias can be explained by (8.6 mm/0.9)(92 days/24 days) = 37 mm of

625   mean upward displacement amplitude, which is a plausible value for the area during active-layer freeze back (Gruber, 2020).

The no-snow intervals are of interest because they serve as a control set with known zero ΔSWE. These show a bias of +1.7 mm which is unexpected since the snow-free period is expected to correspond to subsidence and therefore a negative bias with magnitude similar to but less than Oct-Dec because the subsidence is expected to occur over a longer time-interval than the re-freeze. This disagreement suggests other factors that are difficult to separate from one another; perhaps the thaw

630   is directionally asymmetric with the heave (i.e., contribution from solifluction) as described in Sect. 5.3. The RMSE of the no-snow set is 4.2 mm which serves as a measure of the estimation uncertainty due to factors other than SWE inhomogeneity.

The Apr-Jun intervals are included for completeness even though these are not expected to agree because this corresponds to the snow melt period. This is especially apparent for the two intervals with large negative ERA5 ΔSWE values corresponding to periods of intense snow melt. The SlopeVar estimates for these periods are near-zero, likely because only snow-free areas (snow

635   already melted) are coherent and hence contribute to the estimates and seasonal active-layer thaw has not yet commenced.

6.4 Spatial Distribution of the Estimated ΔSWE

Spatial variations in the estimated ΔSWE maps are due to a combination of true ΔSWE spatial variations, stochastic error due to decorrelation and spatially variable biases as described in Sect. 5. An independent set of densely sampled ΔSWE measurements over our study area does not exist which precludes direct estimation of the errors. Instead, we compare tempo-

640   rally averaged seasonal subsets of the estimated ΔSWE maps since we expect the bias to differ between seasons. Figure 16 shows the temporal mean ΔSWE maps for the early snow season (Oct-Dec), late snow season (Jan-Mar) and all snow-free intervals. These show a moderate degree of negative correlation between the Oct-Dec and snow-free maps, especially in the upland area east of the delta-margin. The Pearson correlation coefficients between the three maps are: $\{R_{\text{Oct-Dec/Jan-Mar}} = 0.28;$ $R_{\text{Oct-Dec/Snow-free}} = -0.52; R_{\text{Jan-Mar/Snow-free}} = -0.17\}$. These are consistent with a dominant bias contribution from surface normal

645   heave and subsidence contributing to the Oct-Dec and snow-free subsets but with opposite polarity. The weaker correlations between these and the Jan-Mar subset suggest a weaker surface-normal bias contribution during this period which is consistent with the expected annual cycle of active-layer heave and subsidence.

Since the snow-free maps have known ΔSWE of zero, a global RMSE value can be computed. This value, computed over all non-water areas and all snow-free maps is $RMSE_{\text{snow-free}} = 21$ mm. We know from Eqs.(13) and (30) that both additive and

650   multiplicative bias contributions are modulated by the local ξ diversity inverse, $\left\langle \tilde{\xi}^2 \right\rangle^{-1}$. We repeated the RMSE calculation for
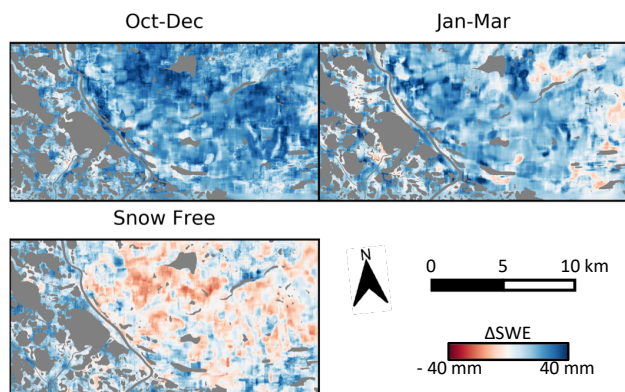
Figure 16. Comparison of mean seasonal ΔSWE maps, showing means for the early snow season (Oct-Dec), late snow season (Jan-Mar) and all snow-free periods (temporal subsets described in Table 3).

the top ξ diversity quartile of spatial samples (corresponding to threshold of $\left\langle \tilde{\xi}^2 \right\rangle^{1/2} > 7.6$ rad mm^{-1}) resulting in $RMSE_{\text{snow-free}}$ = 15 mm which shows that the impact of bias can be reduced by restricting the estimator to areas with greater ξ diversity, albeit with a loss of spatial coverage.

6.5 Correcting for the Dry-Snow Phase Component

655 The main focus of this article is estimation of ΔSWE. However, for repeat-pass InSAR applications other than ΔSWE estimation (e.g. surface deformation estimation), the dry-snow phase can be considered an interfering factor. In this case, knowing the spatial ΔSWE distribution for a given interferogram allows for removal of the snow phase component according to Eq.(5). Furthermore, ΔSWE can, in principle, be estimated at scales finer than the SlopeVar estimation window size by (1) first using SlopeVar to generate a coarse-scale estimate; (2) removing the dry-snow phase corresponding to this initial estimate; and then

660 (3) attributing the remaining InSAR phase to additional (high-spatial frequency) ΔSWE which can then be estimated per resolution cell according to Eq.(5) . We performed a preliminary investigation of this by scaling the estimated ΔSWE maps by the dry-snow phase sensitivity map to generate spatial maps of estimated dry-snow phase and then demodulating the original interferograms. The result was, in general, a significant increase in observed spatial phase gradients and short-scale phase artifacts, likely because of short-scale errors in the estimated ΔSWE maps. This approach therefore requires further investigation

665 because, in order to maintain spatial phase smoothness required for subsequent phase-unwrapping, the ΔSWE maps likely require imposition of smoothness constraints.

6.6 Spatial Resolution

Regarding choice of estimator window size, larger windows improve precision by mitigating the effect of spatially random noise. However, as discussed in Sect. 5, increasing window size does not necessarily mitigate deterministic bias contributions.

670 Therefore, in terms of the trade-off between estimator error and spatial resolution, there is an upper limit for which increasing

window size will significantly reduce the expected error. For our study dataset we empirically determined 500 m to be best choice for the window size since larger windows did not yield significant reductions in the observed spatial variance of ΔSWE estimates.

675   As discussed in Sect. 5.4, the precision of the SlopeVar estimator depends on both the coherence level and the spatial diversity of the SWE sensitivity, summarize by $\left\langle \tilde{\xi}^2 \right\rangle^{1/2}$. These factors are spatially variable and therefore in order to generalize the achievable spatial resolution to other locations one needs to consider both the degree of topographic slope variation and conditions affecting temporal coherence (e.g., vegetation). Within a single dataset, this heteroskedasticity of the estimator could be addressed by applying an adaptively-sized estimation window during the estimation to achieve approximately uniform variance but variable spatial resolution, in other words, growing the window size to compensate in areas of low ξ diversity.

680   Another approach would be to simply mask out areas expected to have high variance based on coherence or ξ diversity.

7   Landcover and Drainage Basin Analysis

A detailed interpretation of the SWE results is not within the scope of this paper, but to demonstrate the advance in estimating SWE over large areas we present a first order assessment of the ΔSWE results in the context of landcover type, fire history, and three drainage basins. To simplify the assessment, we created four major landcover classes by merging the two

685   NALCMS needleleaf forest classes into 'needleleaf forest', the broadleaf deciduous forest and mixed forest classes into 'deciduous/mixed', the two shrubland classes into 'shrubland', and the four grassland or barren classes into 'grassland/barren' (Table 4). We disregard 'wetland', 'urban' and 'water'.

Table 4. Major landcover class fraction for the entire study area and per drainage basin.

	Needleleaf forest	Deciduous/ mixed forest	Shrubland	Grassland/ barren	Other
Study area	0.22	0.30	0.18	0.04	0.27
Basin 1	0.10	0.36	0.38	0.09	0.08
Basin 2	0.31	0.38	0.19	< 0.01	0.11
Basin 3	0.40	0.15	0.39	< 0.01	0.06

To examine the influence of major landcover classes on SWE, we compared their distributions of Oct.-Mar. mean 24-day ΔSWE values across all years (Fig. 17a), and the cumulative mean SWE history per major landcover class (Fig. 17b). The medi-

690   ans of the distributions of Oct.-Mar. mean 24-day ΔSWE values across all years indicate that the windswept grassland/barren unit has the lowest values (12.4 mm). Deciduous/mixed forest and shrub, are similar, 19.2 mm and 17.8 mm respectively, whereas the needleleaf forest is somewhat lower at 16.4 mm. The history of curves for cumulative mean SWE per major landcover class indicate that although cumulative SWE co-varies from year to year among the major landcover classes, each year the grassland/barren area consistently has the lowest cumulative SWE than the other major landcover types. Of the remaining
695 landcover types, deciduous/mixed forest often has the highest cumulative SWE at the end of the winter, with needleleaf forest
and shrub intermediate between the deciduous/mixed forest and grassland/barren.
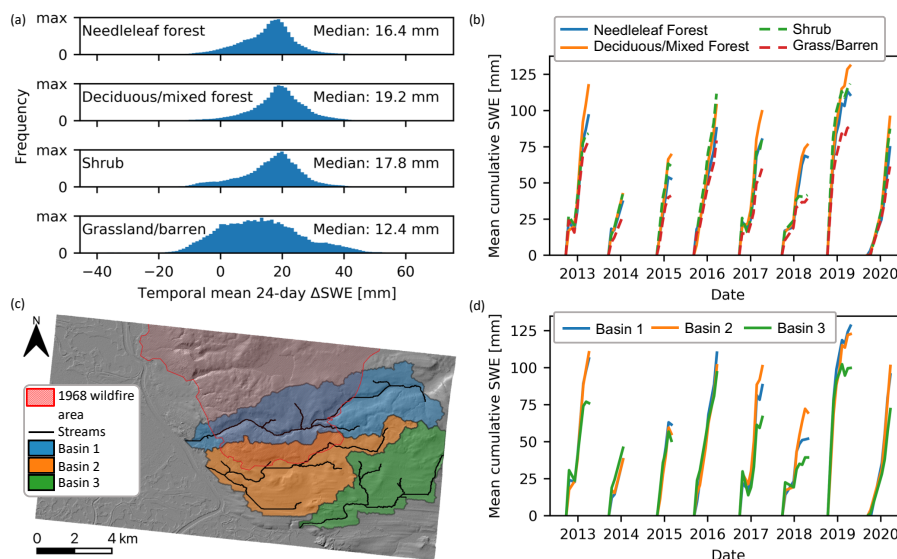
Figure 17. (a) Distributions of Oct.-Mar. temporal mean 24-day ΔSWE according to major landcover class; (b) cumulative mean SWE
histories according to major landcover class; (c) Spatial extent of the three drainage basins analyzed and the 1968 wildfire; and (d) cumulative
mean SWE histories for the non-water areas with the three drainage basins.

Using the SAGA Terrain Analysis tool (Conrad et al., 2015), we demarcated three drainage basins located within our scene
that have similar areas ranging between 22 km² and about 35 km² (Fig. 17c). Landcover class fractions per basin are shown in
Table 4. To compare landcover class areas between drainage basins, we averaged the SWE estimates over the non-water areas
700 (~89 to 95% total basin area) within each basin. Cumulative mean SWE curves (Fig. 17d) show that at the end of the winter,
Basin 3 typically has distinctly less SWE than Basins 1 and 2. Of the three basins, Basin 3 has the highest proportion of old-
growth needleleaf forest, whereas Basin 1 and Basin 2 both have over double the fraction of deciduous/mixed forest. Notably,
the dense deciduous/mixed forest east of Inuvik developed following a major forest-tundra fire in 1968 (extent outlined in Fig.
17c) that burned the widely spaced needleleaf forest (Mackay, 1995), resulting in dense growth of tall alder (*Alnus crispa*)
705 and willows (*Salix spp.*) and regrowth of partly-burned paper birch (*Betula papyrifera*). The 1968 fire completely burned the
forested portion of Basin 1, the forest in Basin 2 was partially burned, but the forest in Basin 3 was beyond the fire limit (Fig.
1c). The SWE data suggest that over half a century since the initial event, the forest-tundra fire near Inuvik is an important
influence on variation in hydrological dynamics in the area, as it is on variation in ground thermal conditions (Palmer et al.,
2012), via ecological succession and its influence on snow cover. The mechanism is not investigated here, but may be related
710 to net radiation and snow ablation in early spring due to the large influx of solar radiation and differences in albedo between
forest and non-forest areas (Rouse, 1984), as at this time of the year the tall shrubs are covered almost completely by snow and
the needleleaf trees stand above the snow cover (Palmer et al., 2012).

8   Conclusions

We have introduced a novel spatial analysis method 'SlopeVar' that estimates dry-SWE change from wrapped repeat-pass
715   interferograms by spatially correlating the InSAR phase to a DEM-derived dry-snow phase sensitivity map over a suitably
sized estimation window. The method does not require phase unwrapping or any spatial reference with known SWE change
and therefore addresses some of the key challenges posed by InSAR-based SWE change estimation.

The method is subject to bias from factors that spatially correlate with the dry-snow phase sensitivity map. We investigated
the role of spatial SWE change inhomogeneity as a possible bias factor by simulating an evolving snow-pack with the Snow-
720   Model snow transport model and found that surface morphology caused sufficient ΔSWE inhomogeneity to generate modest
(few mm of SWE) estimation errors whereas spatial variations in vegetation height (modelled using NALCMS 2015) induced
much larger errors (tens of mm). This leads us to conclude that vegetation homogeneity should be controlled for during esti-
mation, e.g., by limiting the estimator to homogenous areas. We investigated the role of static atmospheric delay and surface
deformation as potential bias factors by correlation with the dry-snow phase sensitivity map. Similarly, we also investigated
725   solifluction and soil moisture phase, two bias sources expected to only affect snow-free interferograms used as zero ΔSWE
controls for method validation. We found that static atmospheric delay and soil moisture are likely not significant sources of
bias and that both surface deformation and solifluction, if present, may lead to substantial estimation bias, generating ΔSWE
errors at scales comparable to the deformation magnitude. We also considered the effect of DEM error and found that DEM er-
rors at scales smaller than the estimation window size lead to damping multiplicative ΔSWE bias and therefore DEM filtering,
730   pre-processing, or both should be performed to minimize this effect.

We tested our method using a 9-year stack of RADARSAT-2 Spotlight-A mode images over an area surrounding the town
of Inuvik, Northwest Territories, Canada and corresponding TanDEM-X DEM for the area. We generated SlopeVar ΔSWE
maps from the dataset for both snow-covered and snow-free periods and compared these with a number of in situ SWE
transect measurements made over two winters and the results showed good agreement with an absolute SWE RMSE of 15 mm.
735   We compared our spatially averaged results with the ERA5 ΔSWE time-history and the results showed a moderately strong
correlation and 7.9 mm RMSE (per 24-day period) over the Oct-Mar period. Seasonal analysis revealed a substantial early
winter (Oct-Dec) bias (8.5 mm per 24-day period) that is largely absent in late winter (Jan-Mar) which we suspect is due to
seasonal active-layer heave.

We empirically determined that a 500 m estimation window size provides the best combination of error mitigation and spatial
740   resolution for our dataset. However, the achievable spatial resolution depends on both terrain factors affecting the coherence
and on the degree of slope variation, both of which are location dependent.

We compared the SlopeVar and Delta-K methods in terms of their relative achievable precision and found that, for our test
area SlopeVar is typically about 4× more precise than Delta-K for a given estimation window size. Regarding the benefits of
the method compared to dual-frequency volume-scattering based estimation, our method is less suitable in areas with relatively
745   low topographic variation, although it may be possible to exploit even sparse areas of variation such as along waterways to
sparsely map SWE change in otherwise flat areas. In other areas the constraints are similar in that they both require dry-snow

conditions and there is opportunity for cross-validation in these areas. Our method has the advantage of only requiring a single band and is therefore feasible with existing spaceborne systems, especially L-band. In comparison to passive microwave-based estimation, assuming dry-snow conditions, we expect the SlopeVar method to perform better in high-relief areas and to be 750 unbiased in areas with high total SWE (> 150 mm), which potentially offers complimentary coverage in alpine regions that have previously been difficult areas to evaluate.

Finally, we applied the ΔSWE results to a first order analysis of accumulation trends by major landcover type and within three drainage basins within the study area and this showed differences between major landcover classes regarding their mean ΔSWE distributions and corresponding multi-year cumulative trends. Differences between basin-level accumulations suggest 755 that re-vegetation following a 1968 wildfire continues to affect the spatial distribution of SWE accumulation in the area.

Author contributions. JE and BR conceptualized the proposed method. JE performed analysis, produced figures and wrote the original draft. JE and PM conducted fieldwork to collect validation data. All authors contributed to the manuscript and editing.

Competing interests. The authors declare that they have no competing interests.

Acknowledgements. Glen Liston provided the SnowModel software used to generate simulated time-evolving SWE distributions. Tim Ensom
760 provided snow survey data. Francesco De Zan provided useful discussions regarding spatial distribution of the dry-snow phase and the possible role of solifluction as an interfering factor. DLR provided the TanDEM-X DEM under science proposal DEM_CALVAL2850. MDA provided the RADARSAT-2 imagery used for the study. The Government of Northwest Territories Department of Environment and Natural Resources provided metrological station data and SWE survey data. This work was funded in part by the NSERC MDA CSA Industrial Research Chair in SAR Technologies, Techniques, and Applications at SFU. This paper is a contribution to the Geological Survey
765 of Canada's Climate Change Geoscience program and is NRCan contribution number 20210443.

References

Anderton, S. P., White, S. M., and Alvera, B.: Evaluation of spatial variability in snow water equivalent for a high mountain catchment, Hydrological Processes, 18, 435–453, https://doi.org/10.1002/hyp.1319, 2004.

Bamler, R. and Eineder, M.: Accuracy of Differential Shift Estimation by Correlation and Split-Bandwidth Interferometry for Wideband and Delta-k SAR Systems, IEEE Geoscience and Remote Sensing Letters, 2, 151–155, https://doi.org/10.1109/LGRS.2004.843203, 2005.

Bekaert, D. P. S., Hooper, A., and Wright, T. J.: A spatially variable power law tropospheric correction technique for InSAR data, Journal of Geophysical Research: Solid Earth, 120, 1345–1356, https://doi.org/10.1002/2014JB011558, 2015.

Burn, C. R. and Kokelj, S. V.: The environment and permafrost of the Mackenzie Delta area, Permafrost and Periglacial Processes, 20, 83–105, https://doi.org/10.1002/ppp.655, 2009.

Burn, C. R., Mackay, J. R., and Kokelj, S. V.: The thermal regime of permafrost and its susceptibility to degradation in upland terrain near Inuvik, N.W.T., Permafrost and Periglacial Processes, 20, 221–227, https://doi.org/10.1002/ppp.649, 2009.

Cong, X., Balss, U., Eineder, M., and Fritz, T.: Imaging Geodesy—Centimeter-Level Ranging Accuracy With TerraSAR-X: An Update, IEEE Geoscience and Remote Sensing Letters, 9, 948–952, https://doi.org/10.1109/LGRS.2012.2187042, 2012.

Conrad, O., Bechtel, B., Bock, M., Dietrich, H., Fischer, E., Gerlitz, L., Wehberg, J., Wichmann, V., and Böhner, J.: System for automated geoscientific analyses (SAGA) v. 2.1. 4, Geoscientific Model Development, 8, 1991–2007, publisher: Copernicus GmbH, 2015.

De Zan, F., Parizzi, A., Prats-Iraola, P., and Lopez-Dekker, P.: A SAR Interferometric Model for Soil Moisture, IEEE Transactions on Geoscience and Remote Sensing, 52, 418–425, https://doi.org/10.1109/TGRS.2013.2241069, 2014.

De Zan, F., Prats-Iraola, P., and Rodriguez-Cassola, M.: On the Dependence of Delta-k Efficiency on Multilooking, IEEE Geoscience and Remote Sensing Letters, 12, 1745–1749, https://doi.org/10.1109/LGRS.2015.2424272, 2015.

Deeb, E. J., Forster, R. R., and Kane, D. L.: Monitoring snowpack evolution using interferometric synthetic aperture radar on the North Slope of Alaska, USA, International Journal of Remote Sensing, 32, 3985–4003, https://doi.org/10.1080/01431161003801351, 2011.

Deems, J. S., Painter, T. H., and Finnegan, D. C.: Lidar measurement of snow depth: a review, Journal of Glaciology, 59, 467–479, https://doi.org/10.3189/2013JoG12J154, 2013.

Derksen, C., Lemmetyinen, J., King, J., Belair, S., Garnaud, C., Lapointe, M., Crevier, Y., Burbidge, G., and Siqueira, P.: A Dual-Frequency Ku-Band Radar Mission Concept for Seasonal Snow, in: IGARSS 2019 - 2019 IEEE International Geoscience and Remote Sensing Symposium, pp. 5742–5744, IEEE, Yokohama, Japan, https://doi.org/10.1109/IGARSS.2019.8898030, 2019.

ECCC: Environment and Climate Change Canada - Canadian Climate Normals, https://climate.weather.gc.ca/climate_normals/, last Modified: 2021-03-25, 2021a.

ECCC: Environment and Climate Change Canada - Historical Data - Climate, https://climate.weather.gc.ca/historical_data/search_historic_data_e.html, last Modified: 2021-07-09, 2021b.

Engen, G., Guneriussen, T., and Overrein, O.: Delta-K Interferometric SAR Technique for Snow Water Equivalent (SWE) Retrieval, IEEE Geoscience and Remote Sensing Letters, 1, 57–61, https://doi.org/10.1109/LGRS.2003.822880, 2004.

Eppler, J. and Rabus, B. T.: The Effects of Dry Snow on the SAR Impulse Response and Feasibility for Single Channel Snow Water Equivalent Estimation, IEEE Transactions on Geoscience and Remote Sensing, pp. 1–23, https://doi.org/10.1109/TGRS.2021.3089131, 2021.

Gruber, S.: Ground subsidence and heave over permafrost: hourly time series reveal interannual, seasonal and shorter-term movement caused by freezing, thawing and water movement, The Cryosphere, 14, 1437–1447, https://doi.org/10.5194/tc-14-1437-2020, 2020.

Guarnieri, A. M. and Tebaldini, S.: On the Exploitation of Target Statistics for SAR Interferometry Applications, IEEE Transactions on Geoscience and Remote Sensing, 46, 3436–3443, https://doi.org/10.1109/TGRS.2008.2001756, 2008.

Guneriussen, T., Hogda, K., Johnsen, H., and Lauknes, I.: InSAR for estimation of changes in snow water equivalent of dry snow, IEEE Transactions on Geoscience and Remote Sensing, 39, 2101–2108, https://doi.org/10.1109/36.957273, 2001.

Hagberg, J. O., Ulander, L. M., and Askne, J.: Repeat-pass SAR interferometry over forested terrain, IEEE Transactions on Geoscience and Remote Sensing, 33, 331–340, https://doi.org/10.1109/TGRS.1995.8746014, 1995.

Hanssen, R. F.: Radar interferometry: data interpretation and error analysis, vol. 2, Kluwer Academic Publishers, 2001.

Harris, C., Kern-Luetschg, M., Murton, J., Font, M., Davies, M., and Smith, F.: Solifluction processes on permafrost and non-permafrost slopes: results of a large-scale laboratory simulation: Full-scale Laboratory Simulation of Solifluction Processes, Permafrost and Periglacial Processes, 19, 359–378, https://doi.org/10.1002/ppp.630, 2008.

Heginbottom, J.: Canada-permafrost, National Atlas of Canada, publisher: National Atlas Information Service, Natural Resources Canada, 1995.

Hersbach, H., Bell, B., Berrisford, P., Hirahara, S., Horányi, A., Muñoz-Sabater, J., Nicolas, J., Peubey, C., Radu, R., Schepers, D., Simmons, A., Soci, C., Abdalla, S., Abellan, X., Balsamo, G., Bechtold, P., Biavati, G., Bidlot, J., Bonavita, M., Chiara, G., Dahlgren, P., Dee, D., Diamantakis, M., Dragani, R., Flemming, J., Forbes, R., Fuentes, M., Geer, A., Haimberger, L., Healy, S., Hogan, R. J., Hólm, E., Janisková, M., Keeley, S., Laloyaux, P., Lopez, P., Lupu, C., Radnoti, G., Rosnay, P., Rozum, I., Vamborg, F., Villaume, S., and Thépaut, J.: The ERA5 global reanalysis, Quarterly Journal of the Royal Meteorological Society, 146, 1999–2049, https://doi.org/10.1002/qj.3803, 2020.

Just, D. and Bamler, R.: Phase statistics of interferograms with applications to synthetic aperture radar, Applied Optics, 33, 4361, https://doi.org/10.1364/AO.33.004361, 1994.

Kokelj, S. V., Palmer, M. J., Lantz, T. C., and Burn, C. R.: Ground Temperatures and Permafrost Warming from Forest to Tundra, Tuktoyaktuk Coastlands and Anderson Plain, NWT, Canada: Permafrost temperatures across tree line northwestern Canada, Permafrost and Periglacial Processes, 28, 543–551, https://doi.org/10.1002/ppp.1934, 2017.

Kunzi, K. F., Patil, S., and Rott, H.: Snow-Cover Parameters Retrieved from Nimbus-7 Scanning Multichannel Microwave Radiometer (SMMR) Data, IEEE Transactions on Geoscience and Remote Sensing, GE-20, 452–467, https://doi.org/10.1109/TGRS.1982.350411, 1982.

Latifovic, R., Pouliot, D., and Olthof, I.: Circa 2010 Land Cover of Canada: Local Optimization Methodology and Product Development, Remote Sensing, 9, 1098, https://doi.org/10.3390/rs9111098, 2017.

Leinss, S., Wiesmann, A., Lemmetyinen, J., and Hajnsek, I.: Snow Water Equivalent of Dry Snow Measured by Differential Interferometry, IEEE Journal of Selected Topics in Applied Earth Observations and Remote Sensing, 8, 3773–3790, https://doi.org/10.1109/JSTARS.2015.2432031, 2015.

Lemmetyinen, J., Derksen, C., Rott, H., Macelloni, G., King, J., Schneebeli, M., Wiesmann, A., Leppänen, L., Kontu, A., and Pulliainen, J.: Retrieval of Effective Correlation Length and Snow Water Equivalent from Radar and Passive Microwave Measurements, Remote Sensing, 10, 170, https://doi.org/10.3390/rs10020170, 2018.

Li, L. and Pomeroy, J. W.: Probability of occurrence of blowing snow, Journal of Geophysical Research: Atmospheres, 102, 21 955–21 964, https://doi.org/10.1029/97JD01522, 1997.

Lin, Y.-n. N., Simons, M., Hetland, E. A., Muse, P., and DiCaprio, C.: A multiscale approach to estimating topographically correlated propagation delays in radar interferograms, Geochemistry Geophysics Geosystems, 11, Q09 002, https://doi.org/10.1029/2010GC003228, 2010.

Liston, G. E. and Elder, K.: A Distributed Snow-Evolution Modeling System (SnowModel), Journal of Hydrometeorology, 7, 1259–1276, https://doi.org/10.1175/JHM548.1, 2006.

Mackay, J. R.: Active Layer Changes (1968 to 1993) Following the Forest-Tundra Fire near Inuvik, N.W.T., Canada, Arctic and Alpine Research, 27, 323, https://doi.org/10.2307/1552025, 1995.

Mackay, J. R. and MacKay, D.: Snow Cover and Ground Temperatures, Garry Island, N.W.T., Arctic, 27, 287–296, https://doi.org/10.14430/arctic2885, 1974.

Matsuoka, N.: Solifluction rates, processes and landforms: a global review, Earth-Science Reviews, 55, 107–134, https://doi.org/10.1016/S0012-8252(01)00057-5, 2001.

Morse, P., Burn, C., and Kokelj, S.: Influence of snow on near-surface ground temperatures in upland and alluvial environments of the outer Mackenzie Delta, Northwest Territories [1] This article is one of a series of papers published in this CJES Special Issue on the theme of *Fundamental and applied research on permafrost in Canada* ., Canadian Journal of Earth Sciences, 49, 895–913, https://doi.org/10.1139/e2012-012, 2012.

Mortimer, C., Mudryk, L., Derksen, C., Luojus, K., Brown, R., Kelly, R., and Tedesco, M.: Evaluation of long-term Northern Hemisphere snow water equivalent products, The Cryosphere, 14, 1579–1594, https://doi.org/10.5194/tc-14-1579-2020, 2020.

Nguyen, T.-N., Burn, C. R., King, D. J., and Smith, S. L.: Estimating the extent of near-surface permafrost using remote sensing, Mackenzie Delta, Northwest Territories, Permafrost and Periglacial Processes, 20, 141–153, https://doi.org/10.1002/ppp.637, 2009.

Nolan, M., Fatland, D., and Hinzman, L.: Dinsar measurement of soil moisture, IEEE Transactions on Geoscience and Remote Sensing, 41, 2802–2813, https://doi.org/10.1109/TGRS.2003.817211, 2003.

Nolan, M., Larsen, C., and Sturm, M.: Mapping snow depth from manned aircraft on landscape scales at centimeter resolution using structure-from-motion photogrammetry, The Cryosphere, 9, 1445–1463, https://doi.org/10.5194/tc-9-1445-2015, 2015.

Oveisgharan, S., Esteban-Fernandez, D., Waliser, D., Friedl, R., Nghiem, S., and Zeng, X.: Evaluating the Preconditions of Two Remote Sensing SWE Retrieval Algorithms over the US, Remote Sensing, 12, 2021, https://doi.org/10.3390/rs12122021, 2020.

O'Neill, H. B., Smith, S., and Duchesne, C.: Long-term permafrost degradation and thermokarst subsidence in the Mackenzie Delta area indicated by thaw tube measurements, in: Cold Regions Engineering 2019, pp. 643–651, American Society of Civil Engineers Reston, VA, 2019.

Pachauri, R. K., Mayer, L., and on Climate Change, I. P., eds.: Climate change 2014: synthesis report, Intergovernmental Panel on Climate Change, Geneva, Switzerland, 2015.

Palmer, M.: Vegetation, snow cover, and air and near-surface ground temperature across treeline in the uplands east of the Mackenzie Delta, Northwest Territories, Master of Science, Carleton University, Ottawa, Ontario, https://doi.org/10.22215/etd/2007-08207, 2007.

Palmer, M., Burn, C., and Kokelj, S.: Factors influencing permafrost temperatures across tree line in the uplands east of the Mackenzie Delta, 2004–2010 [1] This article is one of a series of papers published in this CJES Special Issue on the theme of *Fundamental and applied research on permafrost in Canada* . [2] Polar Continental Shelf Contribution 03611., Canadian Journal of Earth Sciences, 49, 877–894, https://doi.org/10.1139/e2012-002, 2012.

Rabus, B., Wehn, H., and Nolan, M.: The Importance of Soil Moisture and Soil Structure for InSAR Phase and Backscatter, as Determined by FDTD Modeling, IEEE Transactions on Geoscience and Remote Sensing, 48, 2421–2429, https://doi.org/10.1109/TGRS.2009.2039353, 2010.

Rampton, V. N.: Surficial Geology, Tuktoyaktuk Coastlands, District of Mackenzie, Northwest Territories, "A" Series Map 1647A, Scale 1:500,000, Surveys and Mapping Branch, Geological Survey of Canada, 1 sheet, https://doi.org/10.4095/125160, 1987.

Rott, H., Nagler, T., and Scheiber, R.: Snow mass retrieval by means of SAR interferometry, in: 3rd FRINGE Workshop, European Space Agency, Earth Observation, pp. 1–6, Citeseer, 2003.

Rott, H., Cline, D. W., Duguay, C., Essery, R., Etchevers, P., Hajnsek, I., Kern, M., Macelloni, G., Malnes, E., Pulliainen, J., and Yueh, S. H.: CoReH2O, a dual frequency radar mission for snow and ice observations, in: 2012 IEEE International Geoscience and Remote Sensing Symposium, pp. 5550–5553, IEEE, Munich, Germany, https://doi.org/10.1109/IGARSS.2012.6352348, 2012.

Rouse, W. R.: Microclimate of arctic tree line 2. Soil microclimate of tundra and forest, Water Resources Research, 20, 67–73, publisher: Wiley Online Library, 1984.

Saberi, N., Kelly, R., Flemming, M., and Li, Q.: Review of snow water equivalent retrieval methods using spaceborne passive microwave radiometry, International Journal of Remote Sensing, 41, 996–1018, https://doi.org/10.1080/01431161.2019.1654144, 2020.

Sturm, M. and Wagner, A. M.: Using repeated patterns in snow distribution modeling: An Arctic example, Water Resources Research, 46, https://doi.org/10.1029/2010WR009434, 2010.

Takala, M., Luojus, K., Pulliainen, J., Derksen, C., Lemmetyinen, J., Kärnä, J.-P., Koskinen, J., and Bojkov, B.: Estimating northern hemisphere snow water equivalent for climate research through assimilation of space-borne radiometer data and ground-based measurements, Remote Sensing of Environment, 115, 3517–3529, https://doi.org/10.1016/j.rse.2011.08.014, 2011.

Walker, D. A.: Hierarchical subdivision of Arctic tundra based on vegetation response to climate, parent material and topography, Global Change Biology, 6, 19–34, https://doi.org/10.1046/j.1365-2486.2000.06010.x, 2000.

Wessel, B., Huber, M., Wohlfart, C., Marschalk, U., Kosmann, D., and Roth, A.: Accuracy assessment of the global TanDEM-X Digital Elevation Model with GPS data, ISPRS Journal of Photogrammetry and Remote Sensing, 139, 171–182, https://doi.org/10.1016/j.isprsjprs.2018.02.017, 2018.

Zebker, H. and Villasenor, J.: Decorrelation in interferometric radar echoes, IEEE Transactions on Geoscience and Remote Sensing, 30, 950–959, https://doi.org/10.1109/36.175330, 1992.